



**HAL**  
open science

## Experimental validation of a rate-dependent Data-Driven stress Identification method

Adrien Vinel, Rian Seghir, Julien Berthe, Gerald Portemont, Julien Réthoré

► **To cite this version:**

Adrien Vinel, Rian Seghir, Julien Berthe, Gerald Portemont, Julien Réthoré. Experimental validation of a rate-dependent Data-Driven stress Identification method. 2023. hal-04048778v3

**HAL Id: hal-04048778**

**<https://hal.science/hal-04048778v3>**

Preprint submitted on 17 Jul 2023 (v3), last revised 26 Mar 2024 (v4)

**HAL** is a multi-disciplinary open access archive for the deposit and dissemination of scientific research documents, whether they are published or not. The documents may come from teaching and research institutions in France or abroad, or from public or private research centers.

L'archive ouverte pluridisciplinaire **HAL**, est destinée au dépôt et à la diffusion de documents scientifiques de niveau recherche, publiés ou non, émanant des établissements d'enseignement et de recherche français ou étrangers, des laboratoires publics ou privés.

**FULL PAPER**

# Experimental validation of a rate-dependent Data-Driven stress Identification method

Adrien Vinel<sup>1,2</sup> | Rian Seghir<sup>1</sup> | Julien Berthe<sup>2</sup> | Gérald Portemont<sup>2</sup> | Julien Réthoré<sup>1</sup><sup>1</sup>GeM, Centrale Nantes, UMR 6183 CNRS, Nantes, France<sup>2</sup>DMAS, ONERA, F-59014 Lille, France**Correspondence**

Julien Réthoré, GeM, Centrale Nantes, France. Email: julien.rethore@ec-nantes.fr

**Abstract**

The present work proposes an experimental validation of a rate-dependent formulation of the Data-Driven stress Identification method. First the Data-Driven Identification (*DDI*) method is recalled, in its rate-dependent form. A numerical twin of a high speed tensile test applied on non-standard sample geometry is then used to assess the performances of the *DDI*. These performances allow to define confidence intervals depending on multiple indicators (stress magnitude, multi-axiality...). At last, the method is applied to an experiment performed on an XES steel. The kinematic data are retrieved using DIC and then used with the *DDI*. Thus, an experimental estimation of stress tensor fields is achieved. The estimated stresses are then compared with stress predictions using a constitutive equation developed at ONERA.

**KEYWORDS:**DIC ; *DDI* ; Numerical twin ; High strain-rate ; Rate-dependent

## 1 | INTRODUCTION

Iso-static test configurations, usually relying on homogeneous states of strain and stress, have classically been used to characterize (thermo-) mechanical response of materials using various normalized sample geometries (*e.g.* dog-bone (1D), Cruciform (2D)). Indeed, it allows for estimating, in an explicit way, both strain and stress, required to sample the material response, from independent sensors in a purely experimental way. Such tests are historically mono-parametric so a large number of test is required to sample the loading space and particular loading cases can not be properly analysed or analysed at all, including *e.g.* localization processes, strong thermo-micro-mechanical couplings or transient phenomena. Such limitations could be tackled using more complex geometries and/or loading conditions, *i.e.* carrying gradients of all sorts (space and time) and developing original inverse stress field identification methods. Indeed, using the stress field itself as an unknown allows by-passing the use of an *a priori* constitutive equation to analyse such non-isostatic experiments,

contrary to more standard inverse method strategies (*e.g.* Virtual Field Method, Finite-Element Model Updating) which are parametric by nature. In that context, several strategies have been recently adopted to estimate stress fields in non-standard experiments without using a constitutive law. These strategies all rely on full-field measurements and a regularization of the ill-posed mechanical problem, but differ on the chosen regularization.

In 2014, Pierron and his co-authors [31] devised a strategy to estimate stress fields in dynamics (transient load) without using a constitutive law. To this effect, the strategy relies on the use of a statically determined configuration (an inertial impact test for instance). Under the assumptions of plane stress, and a homogeneous and constant density of the material, the authors are able to estimate the mean stress field profile in the specimen. For this strategy, the acceleration acquired experimentally acts as a 1D load cell, which requires recording kinematic fields at ultra-high speed ( $\geq 1\text{M}$  fps). This work opened the way to the so called Image-Based Inertial Impact Tests (IBII). Among other, it allowed the authors to identify the elastic modulus and tensile strength of brittle materials, such as tungsten carbide cermets [10] and composites [12], at



high strain-rate. More recently, the strategy was also applied in a new experimental configuration: the Image-Based Inertial Release (IBIR) test [11]. This new configuration was used to identify both quasi-static and high strain-rate elastic modulus and Poisson's ratio of PMMA samples. In these examples, the boundary conditions (purely inertial test and uniaxial) regularize the problem. If the test is not uniaxial any more, the authors proposed an elegant solution in the case of elastic orthotropic material [30].

Even more recently, in 2021, Liu *et al.* [27] and Cameron and his co-author [4] devised another strategy to estimate stress fields without postulating a constitutive equation. Assuming that the material is isotropic, the methods developed by these authors rely on the alignment of the principal directions of stress with strain or strain-rate. This assumption then allows obtaining a mathematically closed problem, and thus the analytical estimation of stresses. These methods have been tested on numerical example and experimentally in [27]. In [4], the authors discuss the range of validity of such an assumption: mainly in isotropic elasticity, plasticity with associative flow rules and for associative flow rules with an isotropic yield function. Furthermore, this method cannot address the problem of elasto-plastic transition where stresses are not aligned with strains anymore and not aligned with plastic strain-rates yet.

The recent developments in computer science and in particular in the data science field, has lead to the emergence of a third kind of strategy relying on data in the past 4 years: the so called Data-Driven approaches. These methods can be used to either solve the direct problem [17] or the inverse mechanical problem [25]. The so called Data-Driven methods were first introduced in the context of computational mechanics by Kirchdoerfer and Ortiz [17, 18]. In their work, the authors replaced the constitutive equation by a minimization process and a material database. A solution is found by minimizing a distance (which they defined) between computed mechanical states (strains and stresses) and a set of admissible material states. The authors then extended their methods to dynamics [19]. These methods called Data-Driven Computational Mechanics are used to solve the direct problem: find the response of structure (strains and stresses) using a set of admissible material states, which has to be found experimentally. This framework was then derived in order to formulate inverse Data-Driven approaches. Hence, in their work Leygue and his co-authors [25, 26] formulated the inverse problem associated to the Data-Driven Computational Mechanics. This new problem aims to estimate stress fields from heterogeneous experiments without having to explicit any constitutive equation. Using synthetic data, the authors demonstrated the ability of their algorithm to estimate admissible stresses in a structure for various loading cases (quasi-static and dynamic

problems) as well as different material behaviours (hyperelasticity, elasto-plasticity). This Data-Driven method was then applied to experimental data by Dalémat *et al.* in [7]. In this study, perforated hyperelastic membranes are submitted to uniaxial tensile tests. In addition, in a recent paper [6] the authors extensively discuss the proper way to handle imperfect experimental data. The authors especially discuss the boundary conditions for imperfectly defined edges and the way to tackle the issue of missing data. More recently, the Data-Driven strategy was applied by Langlois and his co-authors to experiments on history dependent materials [21]. The use of this method enabled them to estimate stress fields during the formation of plastic instabilities such as Pöbner-Lüders bands. In these strategies, the regularization comes from the assumption that the material response lies on a manifold in a constitutive space which is chosen *a priori*. The underlying hypothesis of this method will be presented later-on in this paper. Furthermore, one could imagine combining this method with the IBII method in order to estimate heterogeneous 2D stress fields in transient dynamics without needing load measurements. It has partly been demonstrated, on synthetic data, in [26]

These emergent strategies can potentially help to assess, without making any assumptions, the validity of material constitutive equations outside their calibration domain (*e.g.* heterogeneous tests, localization, with multi-axiality, couplings...). The objective of this paper is to deploy a rate-dependent *DDI* formulation to characterize the yield stress and hardening rate-sensitivity of a mild-steel using a single test. In that context, the Data-Driven Identification formulation and resolution strategy for rate-dependent elasto-plastic materials will first be recalled. Then, a digital twin is built to investigate the ability of such a method to estimate stress fields, and especially its accuracy. At last but not least, the *DDI* is then applied to data obtained during a high speed tensile test performed on a heterogeneous sample made in steel.

## 2 | DATA-DRIVEN IDENTIFICATION METHOD

The inverse Data-Driven Identification method requires both, a rich database of displacement fields (obtained for example with DIC on complex sample geometries), and net external forces (usually obtained with a load cell). Combined with conservation laws (balance of linear and angular momentum), valid whatever the material, it is possible to build a minimization problem where the components of stress fields are the sought field variables. The following section guides the reader up to final formulation of the global minimization problem.

To make the implementation clearer, we use in the following only matrix notation instead of tensorial one. By default, we use  $[\bullet]$  for matrices and  $\{\bullet\}$  for vectors. When indices are explicitly required they are emphasized as followed,  $X_i^j$ , where  $i$  and  $j$  are matrix rows and columns respectively.

While the main ingredients are recalled in details we refer interested readers to [25] where the *DDI* problem was originally introduced. This work is also inspired by the works of Eggersmann and his co-authors [8] where the framework of DDCM was extended for history dependent materials. Furthermore, the modified strategy, regarding the initialization of the problem, proposed in [26] is adopted. Some notations that will be recalled and used in this work was introduced by Langlois and his co-authors in [21]. The problem is formulated here in small strain, however it has already been implemented and used in finite strain in [7, 32]. Moreover, for experimental concerns, we will focus only on plane-stress formalism.

## 2.1 | Static equilibrium problem

The general problem considers a 2D structure made of a deformable material (see Fig. 1). This structure is discretized using a Finite Element mesh with  $N_e$  elements and  $N_n$  nodes and the loading is discretized through  $N_t$  time steps.

Available data are the following:

- $[u]$ : a  $2N_n \times N_t$  matrix collecting nodal displacements obtained from DIC over the domain  $\Omega$ . The dimension

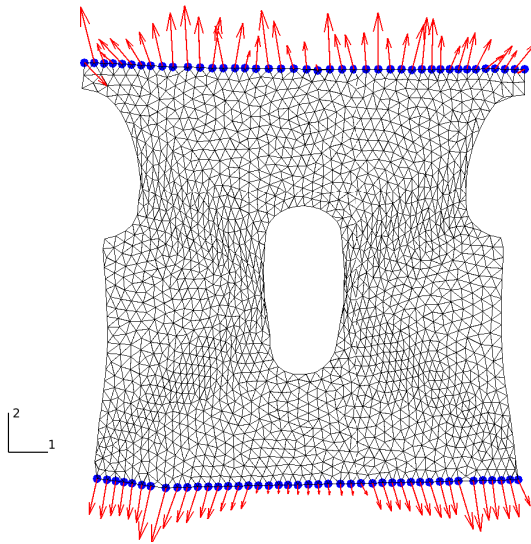


**FIGURE 1** 2D deformable structure made of T3P1 elements over a domain  $\Omega$ . Blue bullets define the border  $\partial F$  where loads and / or displacements are prescribed. Red arrows show a distribution of reaction or applied forces. The configuration is the one adopted for experimental investigation (see Sec. 3).

$2N_n$  means that displacement vectors are organized in vector format such as  $\{u^t\} = \{\mathcal{U}'_1, \dots, \mathcal{U}'_n, \mathcal{V}'_1, \dots, \mathcal{V}'_n\}$  where  $\mathcal{U}$  and  $\mathcal{V}$  are transverse (in the direction 1) and axial (in the direction 2) displacements respectively (see Fig. 1),

- $[B]$ : a  $3N_e \times 2N_n$  matrix obtained from the assembly of elementary FEM gradient operators. The dimension  $3N_e$  encloses the 3 components of the displacement gradient. It is computed using the mesh connectivity and relies on triangular elements and classical linear Lagrange shape functions. It allows for computing strain tensors at every quadrature points, here element centroid noted  $e$ . They are collected in a  $3N_e \times N_t$  matrix:

$$[\epsilon] = [B][u], \quad (1)$$

- $[w]$ : a  $3N_e \times 3N_e$  diagonal matrix collecting the elementary integration weights times Jacobian determinants of the transformation of each element from its reference coordinates frame to its actual shape in the global coordinate system,
- $\{F\}$ : a  $N_t$  vector collecting the net force, along the axial direction 2 (see Fig. 1) of the nodal forces on the upper boundary  $\partial F$ :

$$\{F\} = e \sum_{k \in \partial f} f^t_{N_n+k} \quad \forall t \in [1, N_t] \quad (2)$$

with  $e$  the thickness of the structure, supposed to be constant, and  $[f]$  a  $2N_n \times N_t$  matrix collecting the nodal internal forces.  $N_n+k$  refers to axial displacements only, inline with displacement vector organization.

Static equilibrium can therefore be expressed through a set of  $N_t$  systems of  $2N_n$  linear equations:

$$[B]^T [w]^T \{\sigma^t\} = \{f^t\}, \quad \forall t \in [1, N_t] \quad (3)$$

with  $\sum_{k \in \partial f} f^t_{N_n+k} = \frac{F^t}{e}$  and  $f^t_k = 0, \forall k \in \Omega \setminus \partial F$ .

Considering boundary conditions, especially the fact that only the net force along the axial direction 2 (see Fig. 1) is usually known in practice, and that displacements are prescribed everywhere else on  $\partial F$ , the set of  $2N_n$  equations can be reduced to  $\hat{N} = 2N_n - 4 \text{card}(\partial F) + 1$ . It is implemented by discarding from the system of equation 3 constrained boundary nodes and by adding the linear combination introduced in Eq. 2. It leads to the definition of new condensed operators  $[\hat{B}]$  and  $[\hat{f}]$  summarizing mechanical equilibrium into a compact form:

$$[\hat{B}]^T [w]^T \{\sigma^t\} = \{\hat{f}^t\}, \quad \forall t \in [1, N_t]. \quad (4)$$

## 2.2 | Data-Driven Identification problem

The main idea behind the *DDI* method consists in assuming that a constitutive equation exists, hence there is a constitutive space (still to be defined) where the whole set of mechanical states lies on a manifold. In short, among the infinity of solution of the static problem (see Eq. 4), one seeks for the one that minimizes the spread around an unknown manifold within a well defined constitutive space. Notice that in the following, such a manifold will be approximated by discrete points named material states, in the sense that they literally sample the material response in the constitutive space. Such a discretization allows for regularizing the ill-posed problem of stress identification as we will see later-on.

As a consequence 3 main ingredients have to be defined: (1) such a "well defined" constitutive space, (2) a norm for estimating distances between states in this potentially high dimensional constitutive space, and (3) the sampling of the manifold. The main assumptions of the method are enclosed in these three ingredients.

Constitutive space has to be chosen wisely regarding the various dependencies of the material response to observable and sought quantities. Following Eggersman *et al.* recommendations [8], the history and time-dependent behaviour of the material will be described using strain, stress and their first order time derivatives. To this effect, similarly to what is done in [21], an incremental approach will be used, leading to a dependence of the current stress to the current strain as well as the former strain and stress:

$$\boldsymbol{\sigma}^t = \hat{\boldsymbol{\sigma}}^t (\boldsymbol{\varepsilon}^t, \boldsymbol{\varepsilon}^{t-1}, \boldsymbol{\sigma}^{t-1}). \quad (5)$$

$\hat{\boldsymbol{\sigma}}^t$  will be further used as the *DDI* estimation of the actual stress in this particular space. As a result, and to have same order of magnitude terms within the *DDI* norm (see Eq. 8), the constitutive space that will be considered in this work is  $(\boldsymbol{\varepsilon}^t, \boldsymbol{\varepsilon}^{t-1}, \boldsymbol{\sigma}^t, \boldsymbol{\sigma}^{t-1})$ . From a modelling point-of-view, such a differential constitutive space approaches the material response similarly to rate-dependent plasticity models, classically used in high-strain rate simulation like Johnson-Cook models, which has to be distinguished from visco-plastic models where relaxation time can properly be taken into account.

Then, let us define a distance in a generic strain and stress related constitutive space. Following [17] we choose a norm built from a symmetric positive definite fourth-order tensor  $\mathbb{C}_o$ . Noting for example  $\{\mathcal{P}^t\}$  and  $\{\mathcal{Q}^t\}$ , two vectors related to some strain and stress quantities at time  $t$  respectively in Voigt notation, an energetic  $\|\cdot\|_{\mathbb{C}_o}^2$  norm can be introduced as follows:

$$\|\mathcal{P}^t, \mathcal{Q}^t\|_{\mathbb{C}_o}^2 = \{\mathcal{P}^t\}^T [\mathbb{C}_o] \{\mathcal{P}^t\} + \{\mathcal{Q}^t\}^T [\mathbb{C}_o]^{-1} \{\mathcal{Q}^t\} \quad (6)$$

Normalizing data, such as:

$$\begin{aligned} \{\underline{\mathcal{P}}^t\} &= [\sqrt{\mathbb{C}_o}] \{\mathcal{P}^t\}, \\ \{\underline{\mathcal{Q}}^t\} &= [\sqrt{\mathbb{C}_o}]^{-1} \{\mathcal{Q}^t\}, \end{aligned} \quad (7)$$

the norm simply becomes:

$$\|\mathcal{P}^t, \mathcal{Q}^t\|_{\mathbb{C}_o}^2 = \{\underline{\mathcal{P}}^t\}^T \{\underline{\mathcal{P}}^t\} + \{\underline{\mathcal{Q}}^t\}^T \{\underline{\mathcal{Q}}^t\}. \quad (8)$$

Notice that the square root of the tensor  $[\mathbb{C}_o]$  is computed using an Eigen decomposition,  $[\sqrt{\mathbb{C}_o}] = [V] [\sqrt{D}] [V]^T$ , where  $[V]$  and  $[D]$  are matrices containing eigen vectors and values respectively. Such a normalization will help being more generic, especially avoiding being intrusive for the clustering part of the problem (see Sec. 2.4).

As introduced above, to address the issue of ill-posedness of the stress-field identification problem the material response is discretized with a finite  $N^*$  set of unknown material states  $(\{\boldsymbol{\varepsilon}^*\}, \{\boldsymbol{\varepsilon}^{**}\}, \{\boldsymbol{\sigma}^*\}, \{\boldsymbol{\sigma}^{**}\})$ , where  $\bullet^*$  are related to the current state and  $\bullet^{**}$  to the former state. We will see that these  $N^*$  states are in practice defined as barycenters of mechanical states clusters. These clusters regroup the set of strains and sought stresses  $(\{\boldsymbol{\varepsilon}^t\}, \{\boldsymbol{\varepsilon}^{t-1}\}, \{\boldsymbol{\sigma}^t\}, \{\boldsymbol{\sigma}^{t-1}\})$  that are close in the  $\|\cdot\|_{\mathbb{C}_o}^2$  norm sense. The following form of the *DDI* method can therefore be seen as a zero-order approach in the sense that the regularization introduced by the material states is piece-wise constant.

Considering the constitutive space introduced in Eq. 5, the norm introduced in Eq. 8 and the sampling of the material response into  $N^*$  current and former states, the problem can be formulated as a global minimization:

$$\min_{\substack{\boldsymbol{\varepsilon}^t, \boldsymbol{\varepsilon}^{**}, \boldsymbol{\sigma}^t, \boldsymbol{\sigma}^{**} \\ \hat{\boldsymbol{\sigma}}^t, \boldsymbol{\sigma}^*, \boldsymbol{\sigma}^{**}, S}} \Psi(\boldsymbol{\varepsilon}, \boldsymbol{\varepsilon}^*, \boldsymbol{\varepsilon}^{**}, \hat{\boldsymbol{\sigma}}, \boldsymbol{\sigma}^*, \boldsymbol{\sigma}^{**}, S), \quad (9)$$

where

$$\Psi = \frac{1}{2} \sum_{t=2}^{N_t} \left( \|\mathcal{P}^t, \mathcal{Q}^t\|_{\mathbb{C}_o}^2 + \|\mathcal{P}^{t-1}, \mathcal{Q}^{t-1}\|_{\mathbb{C}_o}^2 \right), \quad (10)$$

with

$$\begin{aligned} \underline{\mathcal{P}}^t &= [\sqrt{p^t}] (\{\underline{\boldsymbol{\varepsilon}}^t\} - [S^t] \{\underline{\boldsymbol{\varepsilon}}^*\}), \\ \underline{\mathcal{P}}^{t-1} &= [\sqrt{p^{t-1}}] (\{\underline{\boldsymbol{\varepsilon}}^{t-1}\} - [S^t] \{\underline{\boldsymbol{\varepsilon}}^{**}\}), \\ \underline{\mathcal{Q}}^t &= [\sqrt{p^t}] (\{\underline{\boldsymbol{\sigma}}^t\} - [S^t] \{\underline{\boldsymbol{\sigma}}^*\}), \\ \underline{\mathcal{Q}}^{t-1} &= [\sqrt{p^{t-1}}] (\{\underline{\boldsymbol{\sigma}}^{t-1}\} - [S^t] \{\underline{\boldsymbol{\sigma}}^{**}\}), \end{aligned} \quad (11)$$

under the constraint that the equilibrium conditions (Eq. 4) are satisfied.  $[p]$  is a  $3N_e \times 3N_e \times N_t$  matrix weighing mechanical states contributions for every time-steps within the functional  $\Psi$ . A specific section (see Sec. 2.5) is dedicated later-on to address the specific role of these weights in the time and space integral.  $[S]$  is a  $3N_e \times 3N_e \times N_t$  selection matrix that maps the  $N^*$  material states to the mechanical states for every

time-steps. Eq. 9 must be understood as the global minimization (time and space) of the scattering of mechanical states around their associated  $N^*$  material states (barycenters) in the particular constitutive space  $(\underline{\epsilon}^t, \underline{\epsilon}^{t-1}, \underline{\sigma}^t, \underline{\sigma}^{t-1})$ .

If equilibrium constraints are enforced using Lagrange multipliers, the following cost function can be obtained:

$$\Phi = \Psi + \sum_{t=1}^{N_t} \left( [\hat{\underline{B}}]^T [w]^T \{ \hat{\underline{\sigma}}^t \} - \{ \hat{f}^t \} \right) \{ \lambda^t \} \quad (12)$$

$\forall t \in [1, N_t].$

Notice that the introduction of normalized quantities " $\hat{\cdot}$ " also requires the normalization of  $\hat{\underline{B}}$  with  $[C_o]$ . It is simply done by assembling normalized gradient operators. Finally, two problems can be formulated: (1) the mechanical and (2) the material one. The stationarity of  $\Phi$  with respect to  $\{ \lambda^t \}$  and  $\{ \hat{\underline{\sigma}}^t \}$  leads to the mechanical problem and the following set of  $N_t$  systems of  $3N_e \times \hat{N}$  equations:

$$\begin{bmatrix} [\hat{\underline{B}}]^T [w]^T & 0 \\ \alpha^t & [p^t]^{-1} [w] [\hat{\underline{B}}] \end{bmatrix} \begin{Bmatrix} \hat{\underline{\sigma}}^t \\ \lambda^t \end{Bmatrix} = \begin{Bmatrix} \hat{f}^t \\ D^t \end{Bmatrix} \quad (13)$$

with,

$$\alpha^t = \begin{cases} 1 & \forall t \in [1, N_t], \\ 2 & \forall t \in [2 : N_{t-1}], \end{cases}$$

$$\{ D^t \} = \begin{cases} [S^{t+1}] \{ \underline{\sigma}^{**} \} & t = 1, \\ [S^{t+1}] \{ \underline{\sigma}^{**} \} + [S^t] \{ \underline{\sigma}^* \} & \forall t \in [2 : N_{t-1}], \\ [S^t] \{ \underline{\sigma}^* \} & t = N_t. \end{cases} \quad (14)$$

Then, the stationarity with respect to the material states leads to the material problem and 4 sets of  $3N^*$  equations:

$$\begin{cases} \sum_{t=2}^{N_t} [S^t]^T [p^t] [S^t] \{ \underline{\epsilon}^* \} & = \sum_{t=2}^{N_t} [S^t]^T [p^t] \{ \underline{\epsilon}^t \}, \\ \sum_{t=1}^{N_{t-1}} [S^{t+1}]^T [p^t] [S^{t+1}] \{ \underline{\epsilon}^{**} \} & = \sum_{t=1}^{N_{t-1}} [S^{t+1}]^T [p^t] \{ \underline{\epsilon}^t \}, \end{cases} \quad (15)$$

Similar equations are used for  $\{ \underline{\sigma}^* \}$  and  $\{ \underline{\sigma}^{**} \}$  respectively. Stationary with respect to  $[S^t]$ , to update the state mapping, is difficult to explicit. Indeed, contrary to other variables, which are continuous numbers of  $\mathbb{R}$ ,  $[S]$  is made of discrete numbers of  $\mathbb{N}$ . As a consequence an alternative method is employed. Details are given in Sec. 2.4.

The resolution of such a problem has already been discussed in [26, 38]. It relies on a staggered algorithm that computes alternatively the Lagrange multipliers and the correction of the stress fields for a given material state set and selection matrices

(called the mechanical problem), then the update of the material states set and selection matrices for given stresses (called the material problem). These two steps are discussed in the next sections.

### 2.3 | Resolution of the mechanical problem

Let us consider a given set of material states :

$(\{ \underline{\epsilon}^* \}, \{ \underline{\epsilon}^{**} \}, \{ \underline{\sigma}^* \}, \{ \underline{\sigma}^{**} \})$  and a given mapping through the selection matrix  $[S]$ .

The mechanical problem can be solved by substitution, leading first to the computation of the Lagrange multipliers:

$$\underbrace{[\hat{\underline{B}}]^T [w]^T [p^t]^{-1} [w] [\hat{\underline{B}}]}_{[M^t]} \{ \lambda^t \} = \underbrace{[\hat{\underline{B}}]^T [w]^T \{ D^t \} - \alpha^t \{ \hat{f}^t \}}_{[b^t]} \quad (16)$$

$\forall t \in [1, N_t].$

It consists in a set of  $N_t$  systems of  $\hat{N}$  independent linear equations to solve. Finally, stresses are updated using the second line of the system of equations 13.

$$\{ \hat{\underline{\sigma}}^t \} = \frac{1}{\alpha^t} \left( \{ D^t \} - [p^t]^{-1} [w] [\hat{\underline{B}}] \{ \lambda^t \} \right), \forall t \in [1, N_t]. \quad (17)$$

### 2.4 | Resolution of the material problem

First, the mapping operator, *i.e.*  $[S]$ , must be computed for given stress fields and the actual set of material states. Finding for each element  $e$  the material state  $N_i^*$  that is the closest with respect to  $\| \cdot \|_{C_o}^2$  is done using k-d tree method. Indeed, since for each iteration of the material problem the database of material state is fixed, efficient space-partitioning data structure strategy can be used to strongly accelerate this operation which remains the bottleneck of the method.

Once this matrix obtained, the set of material states  $(\{ \underline{\epsilon}^* \}, \{ \underline{\epsilon}^{**} \}, \{ \underline{\sigma}^* \}, \{ \underline{\sigma}^{**} \})$  is actualized using Eq. 15. The complexity of the resolution mainly depends on the form of  $[p^t]$ . If  $[p^t]$  is diagonal, as it has always been the case in the literature according the author knowledge, the resolution of Eq. 15 simply consists in computing  $5 \times 3N^*$  independent averages or weighted averages of the mechanical states in elements assigned to each material states through  $[S]$ . For example current and former material strains are found such as:

$$\begin{aligned}
\underline{\boldsymbol{\varepsilon}}_i^* &= \frac{\sum_{t=2}^{N_t} \sum_{j=1}^{3N_e} \left( S_j^i \right)^t \left( p_j^k \right)^t \underline{\boldsymbol{\varepsilon}}_k^t}{\sum_{t=2}^{N_t} \sum_{k=1}^{3N_e} \sum_{j=1}^{3N_e} \left( S_j^i \right)^t \left( p_j^k \right)^t \left( S_k^l \right)^t} \\
\underline{\boldsymbol{\varepsilon}}_i^{**} &= \frac{\sum_{t=1}^{N_t-1} \sum_{j=1}^{3N_e} \left( S_j^i \right)^{t+1} \left( p_j^k \right)^t \underline{\boldsymbol{\varepsilon}}_k^t}{\sum_{t=1}^{N_t-1} \sum_{k=1}^{3N_e} \sum_{j=1}^{3N_e} \left( S_j^i \right)^{t+1} \left( p_j^k \right)^t \left( S_k^l \right)^{t+1}} \\
&\quad \forall i \in [1 : 3N^*]
\end{aligned} \tag{18}$$

The next section discusses the choice of such diagonal  $[p^t]$ .

## 2.5 | Choice of a Weighing matrix

The weighing matrix  $[p]$  of the elementary distance between one mechanical state to its corresponding material state, introduced in the *DDI* norm (see Eq. 8), can be wisely used as a natural filter for noisy experimental inputs. Inputs of the *DDI* being itself an output of the DIC inverse problem, it is necessarily biased and corrupted by noise. Finding a way to mitigate this issue could be valuable for the application of the *DDI* method to real experimental data. Some solutions have already been proposed in the literature for such a weighting matrix.

Evenif it has not been explicitly written as such in literature, two cases can be found: (1)  $[p^t] = \mathbf{I}_2$ , the identity matrix, and (2)  $[p^t] = [w]$  (see *e.g.* [21]). The first solution gives an equal weight to every elements, strain components and time-steps. The authors found it useful when the objective is to identify stresses in vicinity of a localization band using a refined mesh hence where the sought information is localized in space and time. Indeed, the second option, classical for FE integrals, gives more weight to large and undistorted elements discarding data arising from spatial localization. Alternative routes could be used, designing weighting matrix enabling the minimization, for example, of the stress identification noise but this is out-of-the scope of this work. In the following only cases 1 and 2 will be compared.

## 2.6 | Schematic of the global minimization problem

To summarize, the resolution of the global minimization problem, *i.e.* computing  $(\{\underline{\boldsymbol{\varepsilon}}^*\}, \{\underline{\boldsymbol{\varepsilon}}^{**}\}, \{\underline{\boldsymbol{\sigma}}^*\}, \{\underline{\boldsymbol{\sigma}}^{**}\})$ ,  $[\hat{\boldsymbol{\sigma}}]$  and  $[S]$ , is performed using the following staggered algorithm [21]:

1. initialize  $[\hat{\boldsymbol{\sigma}}]$  using a FE simulation with a arbitrary model
2. normalize input dataset to get  $([\hat{\boldsymbol{\sigma}}], [\underline{\boldsymbol{\varepsilon}}])$

3. initialize  $(\{\underline{\boldsymbol{\varepsilon}}^*\}, \{\underline{\boldsymbol{\varepsilon}}^{**}\}, \{\underline{\boldsymbol{\sigma}}^*\}, \{\underline{\boldsymbol{\sigma}}^{**}\})$  and  $[S]$  using a k-means algorithm [28] on  $(\{\underline{\boldsymbol{\varepsilon}}^t\}, \{\underline{\boldsymbol{\varepsilon}}^{t-1}\}, \{\underline{\boldsymbol{\sigma}}^t\}, \{\underline{\boldsymbol{\sigma}}^{t-1}\}) \forall t \in [1, N_t]$ ,
4. solve the mechanical problem (see Sec. 2.3),
5. solve the material problem (see Sec. 2.4), eventually using k-d tree. This step is iterated until convergence of  $[S]$ . It usually takes less than 3 iterations to converge,
6. iterate steps 4 through 5 until convergence of  $[S]$  and  $[\hat{\boldsymbol{\sigma}}]$ . One iteration from step 4 to 5 will be called a cycle.

## 2.7 | Algorithmic parameters

Once the framework of the *DDI* method fixed, meaning that a particular constitutive space (see Eq. 5) and a particular norm (see Eq. 8) are selected, 5 parameters remain to be adjusted by the user and will affect performances of the algorithm.

- the number of material states  $N^*$  sampling the material response
- the amplitude and the exact form of  $\mathbb{C}_o$  within the norm
- the two convergence criteria
- and the weighing matrix  $[p]$

The first one and part of the second one has already been investigated by Dalémat and her co-authors in [6]. They compared the stresses obtained using the *DDI*, considered as the reference, to the ones of FE simulations with different number of material states values. They concluded that a small number of material states leads to an insufficient sampling of the strain-stress manifolds, and thus, to significant error. A high number of material states also leads to significant error, since it will allow outliers to develop and increase the sensitivity to noise (similarly to the overfitting phenomenon for regressions). In their work, the authors recommend a number of material states so that  $20 \leq \frac{(N_t-1) \cdot N_e}{N^*} \leq 100$ . The influence of the magnitude of  $\mathbb{C}_o$  was found to be straightforward as it only intervenes for the clustering step. Eq. 7 shows that by choosing a tensor with high values, the normalization will give more weight to strains compared to stresses. So it may be relevant for the robustness of the clustering to use high amplitude to give more weight to strains which are obtained experimentally, compared to stresses which are unknowns and change during the method.

While the influence of the magnitude of  $\mathbb{C}_o$  is straightforward, the influence of the symmetry class of the tensor remains unknown. In the present work, the fourth-order tensor that will be used is a Hooke tensor for an isotropic material, hence its definition will only be dependent of the choice of a pseudo-Young modulus  $E_o$  (the magnitude) and a pseudo-Poisson ratio

$v_o$ . Nevertheless, it seems reasonable to assume that the use of a pseudo isotropic elastic tensor would not necessarily lead to a satisfying clustering, for instance, of an anisotropic behaviour. However, to the author knowledge, the question of the influence of the symmetry class of  $\mathbb{C}_o$  has not yet been investigated and it is not the objective of the present work.

Regarding the two convergence criteria needed for resolution, the following expressions will be considered:

- for the material problem criterion, we use the convergence rate of the data-driven distance  $\Psi$  (see Eq. 9) at each iteration  $i$ . That is to say:

$$\frac{|\Psi_i - \Psi_{i-1}|}{\Psi_0} \geq \epsilon_{mat} \quad (19)$$

where  $\Psi_0$  is its initial value and  $\epsilon_{mat}$  the user criterion

- for the mechanical problem criterion, we use the convergence rate of the sum (space/time) of the norm of internal force vectors (See Eq. 4). That is to say:

$$\frac{|\mathcal{F}_i - \mathcal{F}_{i-1}|}{|\mathcal{F}_0|} \geq \epsilon_{mech} \quad (20)$$

with,  $\mathcal{F} = \sum_{t=1}^{N_t} \sum_{e \in \Omega} |[\hat{B}]^T [w]^T \{\hat{\underline{\sigma}}^t\}|^2$

Regarding the weighing matrix two options will be compared in this paper.

$$\mathcal{H}_0: [p^t] = \mathbf{I}_2, \forall t \in [1, N_t],$$

$$\mathcal{H}_1: [p^t] = [w]$$

Inputs	Outputs	Parameters	Assumptions
$[u_{dic}], \{F\}$	$[S]$	$\mathbb{C}_o$	Plane stress
$[B]$	$[\hat{\sigma}]$	$N^*$	Small strain
$[\sigma_{fe}]$	$\{\epsilon^*\}, \{\epsilon^{**}\}$ $\{\sigma^*\}, \{\sigma^{**}\}$ $\Psi$	$\epsilon_{mat}, \epsilon_{mech}$ $[p]$	Constitutive space

**TABLE 1** Summary of the inputs, outputs, parameters and the assumptions needed for the Data-Driven Identification method proposed in this work. In this table,  $\Psi$  gives the *DDI* distance at convergence.

Table 1 summarizes the inputs, outputs, parameters and assumptions needed for the proposed Data-Driven Identification method. It emphasizes the fact that, even if *DDI* presents itself as a model-free technique for fields of stress tensors estimation, part of the modelling framework is hidden in the choice of the constitutive space. Nevertheless, while the framework is constrained, the exact form of the constitutive equation

remains free. Moreover, the role of user parameters remains significant and many aspects have still to be investigated. The three main outputs of the method are useful in different ways:

1. The value of the converged *DDI* distance  $\Psi$  gives information about the quality of the stress solution. Indeed, if the scattering remains high the distance will be high emphasizing either issues with input noise, user parameters or the dimensionality of the constitutive space. A proper analysis of this distance may help to improve the constitutive space. Indeed, if relevant dimensions are not taken into account, *e.g.* temperature in a test where an external heat source imposes very high thermal gradients, it will lead to a significant scattering of the data within the chosen sub-space.
2. Mechanical points allow for probing locally (time and space) the mechanical response allowing to access mechanical response in never-seen loading conditions but remain as for DIC, potentially noisy.
3. Material states average the mechanical response and sample, within the constitutive space, an underlying constitutive equation. This quantity could eventually be used to identify a parametric form of the material's behaviour.

### 3 | EXPERIMENTAL METHOD

The *DDI* method has been presented and detailed previously. In this section, the experiment investigated will be presented. It consists in a high-speed tensile test performed on a metal sheet with a specific geometry.

#### 3.1 | Material

The material chosen for this experimental campaign is the rate-dependent, low-carbon mild-steel XES (French standards). Its chemical composition is presented in Tab. 2. The quasi-static and dynamic behaviour of this material are relatively well-known. Indeed, for example in the mid 90s, methodologies were developed allowing to perform double-shear experiments on thin metal sheet in both quasi-static and high strain-rate conditions with highly homogeneous stress and strain states [13]. These methodologies were used to study the shear behaviour of the XES steel – in particular the evolution of the rate sensitivity, for strain-rates ranging from  $10^{-3}$  to  $10^3$   $s^{-1}$  [20]. The tensile behaviour of this steel has also been investigated. For this purpose, Haugou and his collaborators [14] developed a tensile testing device for split Hopkinson bars. This device allows for non-direct tensile tests to be performed on metal sheets. The configuration was used to characterize the mild-steel for strain-rates between  $180$   $s^{-1}$  and  $440$   $s^{-1}$ . At last,

more recently, some researchers focused on the modelling of spot weld for this material. For instance, using experiments based on Arcan principle, Langrand *et al.* [22, 23] were able to model and characterize the joint when submitted to pure and mixed tensile/shear loads in both quasi-static and dynamic conditions. In 2016, Markiewicz *et al.* [29] went one step further and investigated the behaviour of the material when heat affected by spot welding. Furthermore, the authors studied the strain-rate dependency of the heat affected material and identified parameters (see Tab. 3) for a modified Krupkowsky model [33], which is a rate-dependent hardening flow model describing the complex rate-sensitivity of the material. This model is written as:

$$\sigma_{KR} = KX^a (\epsilon_0 X^b + \epsilon_p)^{nX^c}, \quad (21)$$

with  $X = \frac{\dot{\epsilon}_p}{\dot{\epsilon}_0}$ ,

where  $K$ ,  $a$ ,  $b$ ,  $c$ ,  $n$ ,  $\epsilon_0$  and  $\dot{\epsilon}_0$  are the model parameters to be identified. It is inspired from the the Krupkowski hardening flow model (also named Swift hardening model) [39], widely used in FEM softwares, itself inspired from the Hollomon (or Ludwig) hardening flow model [15], both used to model quasi-static mechanical responses in plastic regime. Notice that, at the limit of zero strain-rate, modified Krupkowsky model tends to its peer. It translates the complex relationship between plastic yield, hardening and strain-rate that a more simple model, *e.g.* Johnson-Cook, can not capture. Fig. 2 shows the uniaxial mechanical response of XES for various strain-rates with the fitted model.

### 3.2 | Specimen geometry

Inverse methods for mechanical characterization allow for using complex sample geometries which will no longer lead to homogeneous fields and cover for example large spectra of strain and strain-rates in a single experiment. The question of their design is extremely vast. It can be based on an heuristics approach starting from standard geometries (see *e.g.* [3, 16]) or using proper optimization approaches, such as *e.g.* constrained topology optimization [2, 5]. In this work, the first approach is considered and the chosen specimen geometry is simply derived from the one classically used when using a hydraulic tensile test machine (see the next section for more details). Indeed, the use of such a device limits the specimen length and width. In addition, since the *DDI* method needs the load recorded by the load cell, the sample needs to admit the loading axis as a symmetry axis in order to avoid the introduction of any bias in the load measurement (*e.g.* transverse loading).

The main features of the geometry are two symmetrical notches and a central hole (see Fig. 3). Such features are expected to lead to strain concentration bands between the notches and the central hole as well as secondary bands from

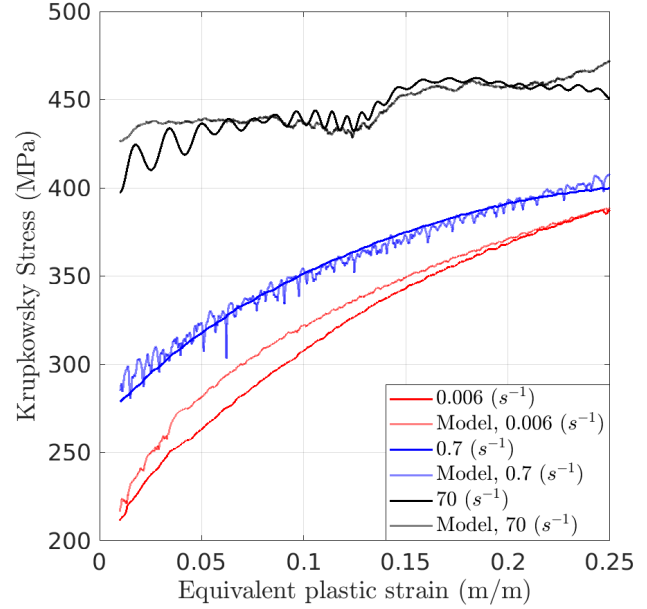


**FIGURE 2** Reference data and modified Krupkowsky model previsions from [29] obtained during high strain-rate tensile tests.

the central hole to the edge of the sample with an angle of approximately  $45^\circ$ . The specimens were cut from a 0.8 mm-thick metal sheet in the rolling direction.

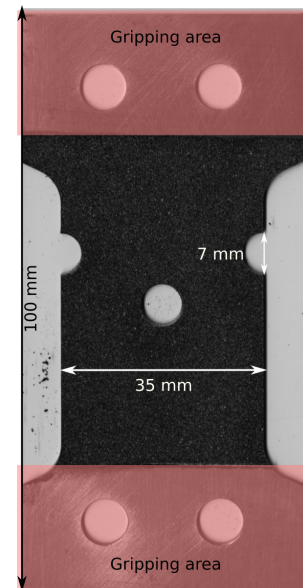


**FIGURE 3** Photography of a sample, its principal features are two symmetrical notches and a central hole.



C	S	N	Mn	P	Si	Al	Ni	Cr
0.0268	0.0175	0.006	0.202	0.007	0.007	0.07	0.018	0.036
Cu	Mo	Sn	Nb	V	Ti	B	Ca	
0.014	0.002	0.004	0.001	0.002	0.002	$\leq 0.0003$	$\leq 0.0003$	

**TABLE 2** XES chemical composition (in wt%), data from [29].

Parameters	$K$ (MPa)	$\epsilon_0$	$n$	$\dot{\epsilon}_0$ ( $s^{-1}$ )	$a$	$b$	$c$
[29]	526.6	0.024	0.221	0.085	0.0002	0.385	0.002

**TABLE 3** Parameters for the modified Krupkowsky model from [29].

### 3.3 | Experimental setup

The tests conducted in this work are high speed tensile tests. They are conducted using a hydraulic tensile test machine (MTS-819, 20 kN). On this machine, the upper grip is mounted on a modified Hopkinson bar, similarly to the device from [24]. This bar is made of steel (42CD4 rectified) and is instrumented with strain gauges in order to act like a load cell (see Figure 4). In addition, the lower grip is mounted on a sliding bar. The sliding bar is in an enclosing case linked to the actuator. The sliding bar, through the control of the “free fall” length, allows the actuator to reach the imposed displacement speed before loading the sample. The maximum actuator velocity allowing an accurate load measurement, *i.e.*  $5 \text{ m s}^{-1}$ , is used for this experiment. The “free fall” distance was accordingly set to 25 mm.

### 3.4 | Imaging setup

The visible wavelength camera used in this work is the high-spatial resolution ultra-high speed (HR-UHS) Cordin-580. It is a rotating mirror camera that captures 78 images of 8 megapixels ( $2472 \times 3296$  pixels) up to 4 million fps. This camera and its specificities have been studied in depth in [41] (see appendix A for more details). For the experiment presented in this work, the camera is equipped with a 90 mm Tamron objective, and records at 68 kfps with a CDS gain of -3 dB (Correlated double sampling) and a CCD gain of 15 % (amplification factor in the analog-to-digital converter). At such speed, the film duration is about 1.18 ms. Such a “low” frame-rate has been selected with regards to the infrared camera capabilities used to capture temperature fields (see below). In order to provide enough light, two Pro-10 (2400 J each at 10-stops) Xenon flashes from Profoto are used. They are set in normal mode, at 10 f-stops. In that configuration, the illumination typically lasts 2.4 ms with a stable and optimal plateau of 1.1 ms. The flashes and the camera are triggered separately in this experiment. The flashes are triggered using an infrared light-gate system (SPX1189 series

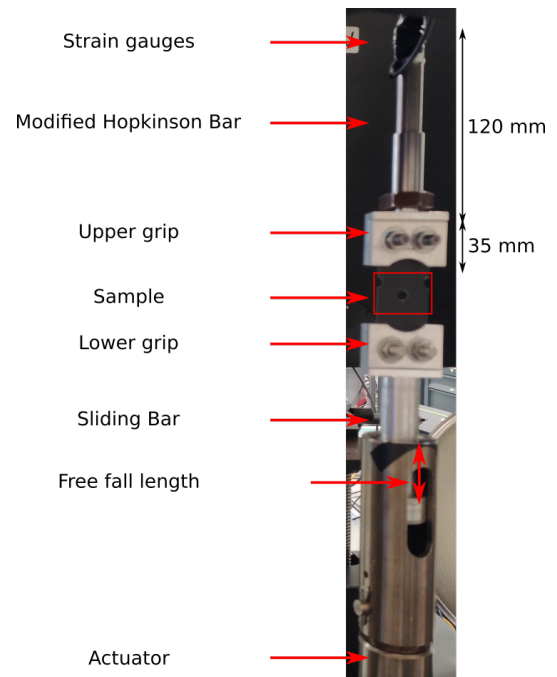


**FIGURE 4** Close-up view of the high speed tensile machine setup.

Honeywell). It is placed in such manner that it is obscured by the enclosing case. The optical gate will then send a 5 V TTL signal when the enclosing case is at a given distance to the contact with the sliding bar. This distance has to take into account the speed of the actuator as well as the rising time of the flashes ( $150 \mu\text{s}$ ). It has been empirically determined and set at 3.7 mm from the contact point. The Cordin-580 is triggered using the load cell. When the load reaches a chosen threshold (in this study  $6231.5 \text{ N}$ ,  $\approx$  half of the plastic yield), a trigger is sent to the camera. Upon receiving the trigger, the camera will record the following images, as well as the ones taken up to  $100 \mu\text{s}$  before (this is named post-triggering). These parameters were determined empirically through preliminary tests. Furthermore, the working distance between the camera and



the sample is about 31 cm, leading to a pixel size of  $14.49 \mu\text{m}$ . These information are summarized in Tab. 4.

An high-speed infrared camera (a Telops M3K) is also used to record the other face of the sample during the experiment (see Fig. 5). The infrared results fall out of the scope of the presented work. Nevertheless, thermal information confirmed that no strong thermomechanical couplings are induced by the strain. Indeed, mean sample temperature rises up to  $5^\circ\text{C}$  while the temperature within localization band does not exceed  $50^\circ\text{C}$  before fracture onset. It confirms that the constitutive space used to identify stresses does not have to take into account explicitly temperature (see Sec. 2).

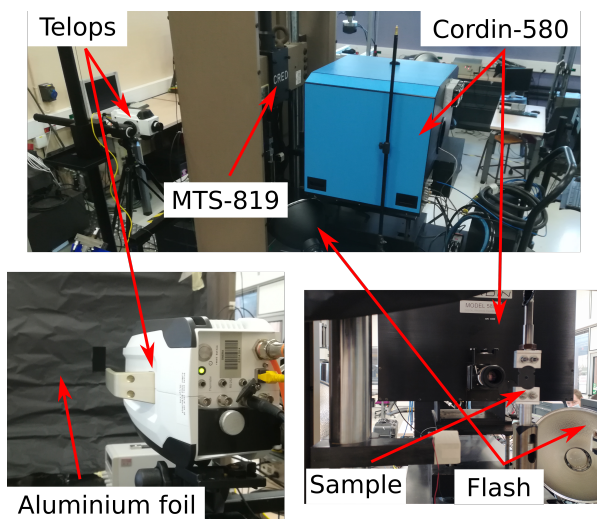


**FIGURE 5** Experimental setup for a high speed tensile test, recorded using a visible-light camera and an infrared one.

### 3.5 | DIC setup and parameters

In order to be able to perform DIC on the images recorded by the camera an undistorted reference image is needed. Indeed, rotating mirror cameras produce distorted images and requires an absolute reference for DIC (see appendix A for more details). In this work, this image is obtained by recording, prior to the test, images of the sample at rest with its black and white paint speckle-like pattern using a high definition camera (29M pix, Prosilica GT from Stemmer) combined with the same objective lens. The image is eventually down-scaled to the Cordin camera resolution. Furthermore, following this methodology, 12 calibration shots were taken with the Cordin camera when the first sample was mounted, prior to the test. These calibration shots are used in order to create a representative model of the distortions induced by the camera in experimental conditions (lens, working distance, magnification, frame rate). Then, in order to correct the eventual rigid body motion between one experiment and the other, a single calibration shot is performed before each of the other experiments. See [41] for more details regarding the entire recently developed dedicated DIC framework.

In this work, a finite element description of the displacement field is used. Since it is known that strain localization appears in 2 principal bands, the mesh is refined along these bands and in the vicinity of the notches and the hole as well. The element size is 32 pixels on average, but finer along the crack (about 26 pixels). A Tikhonov regularization of the DIC problem of  $4 \times 32$  pixels is used to filter-out spatial noise. The displacements are firstly pointwise convolved with a moving temporal Savitzky-Golay filtering window of second order with a window size equal to 23 frames (see Tab. 5). Then strain-rates are obtained from strains using a simple  $1^{st}$  order finite difference scheme. Such data filtering marginally affects strain, but significantly decreases the level of noise on strain-rates.

Camera	Cordin-580
Image resolution	$2472 \text{ pixels} \times 3296 \text{ pixels}$
Dynamic Range, Detector	12 bits
Dynamic Range, Image	16 bits
Acquisition Rate	68 kfps
Lens	Tamron SP 90 mm Di Macro
Aperture	$f/2.8$
Field of view	$35.8 \text{ mm} \times 47.8 \text{ mm}$
Image scale	$1 \text{ pixel} = 14.49 \mu\text{m}$
Stand-off distance	31 cm
Patterning Technique	Black and White paint

**TABLE 4** DIC hardware parameters.

DIC Software	Ufreckles [34]
Shape Function	linear FE triangular elements
Matching Criterion	ZNSSD
Image Filtering	sensor flattening (vignetting)
Data Processing	$U$ : Tikhonov regularization over $4 \times 32$ pixels
Data Post-Processing	$\dot{\epsilon}$ : Savitzky-Golay filter of order 2 applied onto $U$ (win = 23 fr)

**TABLE 5** DIC analysis parameters.

### 3.6 | Technical issues and solutions

Due to the complexity of the experiments conducted, some technical issues have to be tackled. This is the aim of this section.

#### Load measurement

The load is captured by the load cell during the experiment. However, it has to be adjusted time-wise: indeed, the load is measured by strain gauges while the information is needed on the mesh boundary, in particular for the *DDI* (see Sec. 2). Hence, due to the distance between the mesh boundary and the strain gauges, a delay has to be taken into account. Figure 4 presents the experimental apparatus, with in particular the distances of interest: the distance between the strain gage and the grip (120 mm using the constructor's data) as well as the distance between the grip and the ROI ( $\approx 35$  mm measured manually). Then, using the modified bar's properties ( $E = 205$  GPa and  $\rho = 7850$  kg/m<sup>3</sup>), the delay is computed as follows:  $\tau = \sqrt{\frac{\rho}{E}}$ , which yields a delay of 30  $\mu$ s. This is in the order of magnitude of two Cordin interframes for this experiment. Furthermore, note that even an error of 1 cm in the distance between the grip and the ROI leads to an error of 2  $\mu$ s for  $\tau$ , which is negligible regarding our time resolutions.

#### Pre-stressed sample

The experimental setup is hyper-static, and as a result, the sample when fixed is already pre-constrained. Indeed, the gripping device relies on two metallic rods on each side of the sample to maintain it. However, due to its use, the rods are slightly deformed. As a result, the sample may be already slightly stretched when put in place before the experiment. Thus, the loading is slightly non symmetrical, which will explain why the crack systematically starts always on the left-hand side. Nevertheless, this phenomenon is not significant. Moreover, since the reference image is obtained before the test outside of the setup, contrary to standard procedure for DIC where the first image is usually the first frame of the test shot, any pre-stretch is measured.

#### Influence of the flashes

The requirements for ultra-high speed DIC imaging and infrared measurements around room temperature are antagonistic. Indeed, a large amount of light is required for the UHS imaging, which usually covers a large spectrum of wavelength, while the IR measurements require no disturbances within its wavelength bandwidth of recording.

Tests were conducted in order to investigate the flashes influence on the temperature measurement. To this effect, a blackbody was placed at the sample's location and was set at 25 °C while the other experimental conditions remained the

same (IT, fps, windows size and the aluminium foil was also used) in order to be as representative as possible. Then, the flashes were activated manually and the thermal scene was recorded. This procedure has been performed twice. It has been observed that the flashes, due to their light being emitted partially in the infrared range recorded by the IR camera, induce an apparent rise of temperature captured by the camera. Since this phenomenon is very reproducible, a correction is applied to the experimental temperatures in order to retrieve the effective sample's temperature. The systematic and random errors obtained after the correction are  $0\text{ °C} \pm 0.230\text{ °C}$ . This may compromise the proper measure of thermo-elastic effects which are in the same order of magnitude in the case of metals.

## 4 | METROLOGICAL ASSESSMENT USING A NUMERICAL TWIN

In order to investigate the *DDI* method introduced in Section 2 and the influence of the user parameters, a numerical validation is conducted and is presented in this Section. Note that, contrary to classical 1D loading cases, the presented work relies on data existing in a 12-dimension space (3 for  $\epsilon$ , 3 for  $\dot{\epsilon}$ , 3 for  $\sigma$ , 3 for  $\dot{\sigma}$ ). Such high dimensionality requires developing new ways to display results. Nevertheless, such developments go beyond the scope of this work. Hence, for the sake of simplicity the majority of the results will be presented in sub-spaces using invariant based norms (*e.g.*  $I_1$ ,  $\sqrt{3J_2}$  or Von-Mises). Note that this is not a requirement but just a choice. Any other norms or invariants could have been chosen.

### 4.1 | Creation of a Numerical twin

The construction of a numerical twin of the experiment, allows to have access to a realistic estimation of the data that will be measured during the real experiment. Furthermore, it allows to qualify an experiment in terms of measurability of the fields of interest (in the present case the stress tensors), and their uncertainties. It can also validate an identification procedure and its robustness with respect to realistic experimental conditions. In order for this procedure to be relevant, VID must take into account, as much as possible and as accurately as possible, experimental errors and uncertainties such as:

- The spatial resolution of the imaging system and the DIC sampling, which affects the ability to capture strain gradients,
- The temporal resolution of the imaging system, which affects the temporal derivatives (speed, acceleration),

- The bias induced by the camera (in our particular case, when using the Cordin, the bias induced by the camera's distortions which lead to low but still non-negligible displacement errors),
- Sensor noise, which affects the optical flow in DIC and thus displacement errors as well as time derivatives.

Obviously such procedure is never perfect, for instance, it is difficult to take into account strong speckle-like pattern transformation or even degradation in highly deformed regions during large strains [42], light variation, out-of-plane motions... However the use of VID is becoming more and more systematic in the validation of an experimental procedure and of inverse identification methods [36, 1, 35, 16, 3, 37, 10, 30, 9].

Thus, in the following paragraphs, this construction is described. Several Finite-Element simulations will be performed using Abaqus with the implicit solver using CPS3T elements. In all the FE simulations the thermomechanical Johnson-Cook model will be used as it is implemented by default in FE solvers.

It is important to note that the VID has to take into account the specificities of the chain of measurement in order to be as close as possible to the experimental conditions. Thus in our case, the specificities of the Cordin-580 (which are briefly recalled in Appendix A) will be taken into account since it introduces low but non-negligible displacement errors. Nevertheless, the methodology can be used with all the different existing technologies.

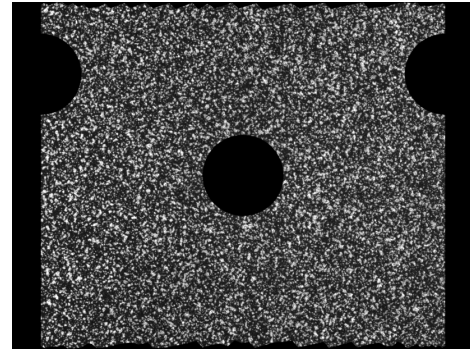
#### Creation of a reference solution ( $U^{\text{ref}}$ , $\sigma^{\text{ref}}$ , $F_y^{\text{ref}}$ )

A FE simulation is first performed in order to create a reference solution, which will serve 2 purposes : (1) the construction of Virtual images, (2) the comparison of the results after using the whole chain leading to the estimation of stress tensors (DIC + *DDI*). This simulation is conducted using the model parameters given in in Tab. 7 (this will be called Model A in the rest of this work). They have been identified using a tensile test at an average strain-rate of  $70 \text{ s}^{-1}$  from a previous study [29]. To mimic the experiments, the simulation is performed under imposed displacements on the upper and lower boundaries. On the upper boundary a 0 displacement fields is imposed in both the axial and transverse directions as it is gripped. On the lower boundary, a displacement corresponding to a velocity of  $5 \text{ m s}^{-1}$  is imposed in the axial direction. For simplicity purposes, this simulation is performed using an experimental DIC mesh that is used for the actual experiment. The same mesh will be used throughout the whole procedure.

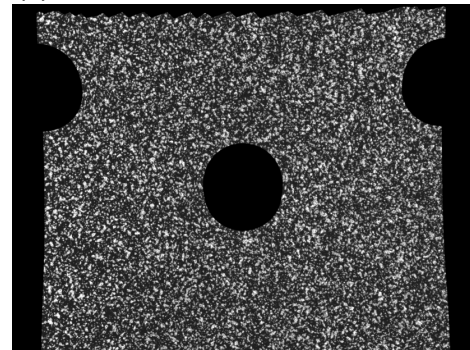
The outputs of this simulation – namely the displacement fields  $U^{\text{ref}}$ , the stress fields  $\sigma^{\text{ref}}$  and the vertical net force on the upper boundary  $F_y^{\text{ref}}$  – will be used as references for what follows.

#### Virtual Image Deformation

In order to be able to perform DIC on the synthetic images, a texture needs to be applied. For this study an experimental image of a spray paint speckle-like pattern covering the entire camera field of view is considered. This reference image is obtained using a high resolution camera then binned down to the Cordin image size. Then, using the same mesh as FE simulation, the pixels out of the sample are disregarded resulting in the image in Figure 6a. The field of view (see Table 6) matches the aspect ratio of the camera for a pixel size of  $14.49 \mu\text{m}$  (*i.e.* a magnification of 0.38).



(a) Reference image created synthetically,



(b) Deformed and distorted image,

**FIGURE 6** Example of the reference image and a deformed and distorted image created synthetically.

Once the reference image created, using the mesh and the displacement fields from the reference simulation, the image is deformed (see Fig. 6b for an example). This is done by performing a loop on the elements of the deformed mesh. For each element, the pixels contained in it are known. Using shape functions and inverse mapping, their position in the undeformed picture is obtained. Their associated grey values can then be retrieved by performing a spatial bi-cubic spline interpolation of the grey value of the reference image. This process is summarized in Figure 7.



**FIGURE 7** Schematic of the deformation procedure of a synthetic image for one triangular element. The black squares depict the pixels positions in the deformed configuration, while the grey squares depict the pixels positions in the reference one. The red crosses denote the pixels from the deformed configuration projected by an inverse mapping in the reference one. The deformed image for the element is obtained by interpolating (bi-cubic spline) the grey levels from the grey squares onto the crosses.

Furthermore, in order to be as representative of a real experiment as possible, measurement bias introduced by the distortion variability from one shot to another has to be taken into account. In practice, two sets of distortion parameters obtained experimentally are used. The first one is used to deform the images and the second one is used to perform DIC. As a result, this allows to introduce the right order of magnitude of error in displacement measurement inherent to the method. Using the composition relationship between the effective displacement  $u_{\text{simu}}$  and the first distortion field  $u_d$ , the imposed displacement  $u_{\text{virtual}}$  used to deform the images is computed as follows:

$$u_{\text{virtual}}(\underline{X}) = u_{\text{simu}}(\underline{X}) + u_d(\underline{X} + u_{\text{simu}}(\underline{X})). \quad (22)$$

Finally, a realistic noise is added to the deformed and distorted synthetic images. The estimation of grey level noise, meaning apparent grey level variation of one material points from one image to another over time, has been estimated as follows:

- Images of a static reference shot of the sample are deformed back to the undistorted configuration using identified distortion parameters.
- The grey level standard deviation over time of every pixel is computed and its normalized value (by the pixel's grey level) plotted as a function of the mean grey level value of the considered pixel. The plot is presented in Figure 8. This evolution can be fitted with a power law  $P$  to get the trend of the apparent noise of the camera over its dynamic. The power law used is depicted in the figure by the black line.
- This result is used to add random noise to images proportional to pixel grey levels following this equation:

$$\text{noise}(F, p) = F(p) \cdot P(F(p)) \cdot \text{randn}(p), \quad (23)$$

where  $\text{noise}(F, p)$  is the noise that will be added to the pixel  $p$  of image  $F$ ,  $P(F(p))$  is the noise magnitude fitted by the polynomial for the considered grey value  $F(p)$  and  $\text{randn}$  is a normally distributed random numbers matrix of the size of  $F$ .

At the first order, the polynomial fit shows that the apparent noise converges toward 5% in the whites, reaches 10% at about 12 bits (4000) then ramps up to 30% in the blacks. Notice that, in practice, data presented in Figure 8 is not strictly speaking a noise. Indeed, pixel time variations are in our case not only due to CCD dark noise but to the offset and gain mismatch from one sensor to another, the focus mismatch, as well as the uncertainty on distortion estimation which does not allow for perfectly stabilizing images ( $\pm 0.1$  pixel). This is why we name it apparent noise. In addition, it explains why values are very high compared to mono-sensor ultra-high speed camera (*e.g.* in the order of 1% of 16 bits for the Shimadzu HPV-X). Nevertheless, apparent noise will affects the optical flow in a similar way to real noise and will have a strong impact on time derivatives.

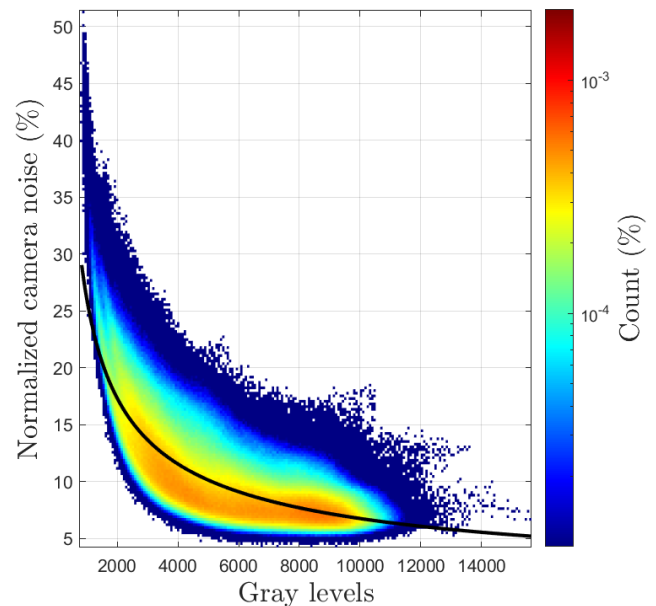


**FIGURE 8** Normalized apparent camera noise (in %) versus the mean grey level. The colour denotes the pixel counts (in %), while the black line denotes the polynomials used to model the camera noise.

As a summary, at this stage we have produced, references kinematic fields as well as images that mimic the response of

our imaging system. Applying the dedicated DIC procedure for the Cordin camera allows for capturing realistic displacement fields  $U^{\text{DIC}}$ . In the next section, the *DDI* method will be used using these fields in order to assess its accuracy as well as the influence of user parameters.

DIC Software	Ufreckles [34]
Image size	2472 x 3296 pixels
Field of view	35.8 mm × 47.8 mm
Cordin pixel size	5.5 μm
Image scale	1 pixel = 14.49 μm (Magnification of 0.38)
Mesh size	≈ 21 pixels
Data Processing	$U$ : Tikhonov regularization over 128 pixels

TABLE 6 Virtual DIC parameters.

## 4.2 | Creation of a statically admissible initial solution using a “wrong” model

The creation of an initial guess for the stress field that will be used as an input for the *DDI* algorithm requires two consecutive Finite-Element simulations. To validate the *DDI* procedure, an initialization reasonably far from the solution is chosen. To this effect, the same model as the reference one is chosen but the constitutive parameters are significantly modified. Hence, the initial yield is decreased, whereas the hardening modulus is increased. In addition, to investigate the ability of the *DDI* to accurately retrieve the strain-rate dependency, the strain-rate dependency is set close to zero. The exact parameters are given in Tab. 7 (it will be called Model B).

- The first simulation is conducted under imposed displacements, using  $U^{\text{DIC}}$ . The load profile on the upper boundary is extracted from this simulation. This profile is then rescaled in such a manner that, in the end, the net force on the upper boundary is equal to the reference net force  $F_y^{\text{ref}}$  for all the time steps. The role of this first simulation is to get a nice estimation of the load distribution at the upper bounds of the sample.
- The second simulation is then performed under mixed boundary conditions: imposed displacements on the lower boundary, imposed displacements in the  $X$  direction and imposed rescaled vertical distribution of forces on the upper bound. This simulation allows to obtain statically admissible stresses  $\sigma^{\text{false}}$ .

The whole procedure is summarized in Figure 9. In what follows the *DDI* will be given the total strains  $\epsilon_t^{\text{DIC}}$  (computed

from  $U^{\text{DIC}}$ ) and  $\sigma^{\text{false}}$  as inputs. This case allows to assess the influence of the measurement errors on the estimation of the stress fields. Hence, the final errors are representative of the ones expected during real experiments.

## 4.3 | Results and discussion

The *DDI* is performed on 50 time steps using simulation results as described previously. First the influence of the different parameters (see Tab. 1) of the *DDI* will be investigated. Then, once the parameters chosen, the *DDI* results will be presented and discussed.

### Influence of the parameters

To investigate the influence of the different parameters of the method, several computations were performed. The number of material states  $N^*$  is chosen so that  $30 \leq \frac{(N_t-1) \cdot N_e}{N^*} \leq 200$ , the ratio  $\frac{E_o}{E}$ , with  $E$  the actual material Young Modulus, varies from 0.1 to 10 and finally the weighting matrices  $[p]$  are either  $\mathbf{I}_2$  or  $[w]$ . In addition a median filter with 0 to 5 neighbours (noted  $l_c$ ) is applied to DIC strains before the *DDI*. In order to assess which quadruplet leads to the best results, the following equivalent standard deviation  $\xi_{\text{eq}}$  is considered:

$$\xi_{\text{eq}}(\sigma_{\text{DDI}}) = \left( \frac{1}{3} \sum_i \text{Var}(\Delta\sigma^i) \right)^{\frac{1}{2}}, \quad i \in \{1, 2, 6\}, \quad (24)$$

$$\Delta\sigma^i(e, t) = \sigma_{\text{DDI}}^i(e, t) - \sigma_{\text{ref}}^i(e, t) \quad (25)$$

Thus, the error is the square root of the variance of the difference between the identified stresses and the reference ones for all the elements and time steps, averaged over the three components. This error allows in one scalar to take into account each component of the stress tensors for all the elements and all the time steps.

The best parameters among those tested are the following :  $N^* = \frac{1}{30}(N_t - 1) \cdot N_e$ ,  $E_o = 10.0 \cdot E$  where  $E$  is the steel's Young modulus,  $l_c = 2$  and  $[p] = [w]$ . Figure 10 depicts the evolution of  $\xi_{\text{eq}}$  when 3 out of 4 parameters are fixed and one varies. This figure shows that the error increases when the number of material states decreases. Furthermore, the error decreases when  $E_o$  increases. These trends are in line with the observations from [6]. In addition, this figure highlights that there is an optimal filtering length for DIC strains:  $l_c = 2$ . At last but not least, the choice of the weighting matrices do not have a significant influence on the error. Nevertheless, the use of  $[w]$  leads to a small reduction of the error (from 24.8 MPa to 23.7 MPa).

### A posteriori filtering operator

Let us consider the identified mechanical points distribution in the  $\{\|\epsilon\|_{VM}, \|\sigma\|_{VM}\}$  space. This space is of interest since it

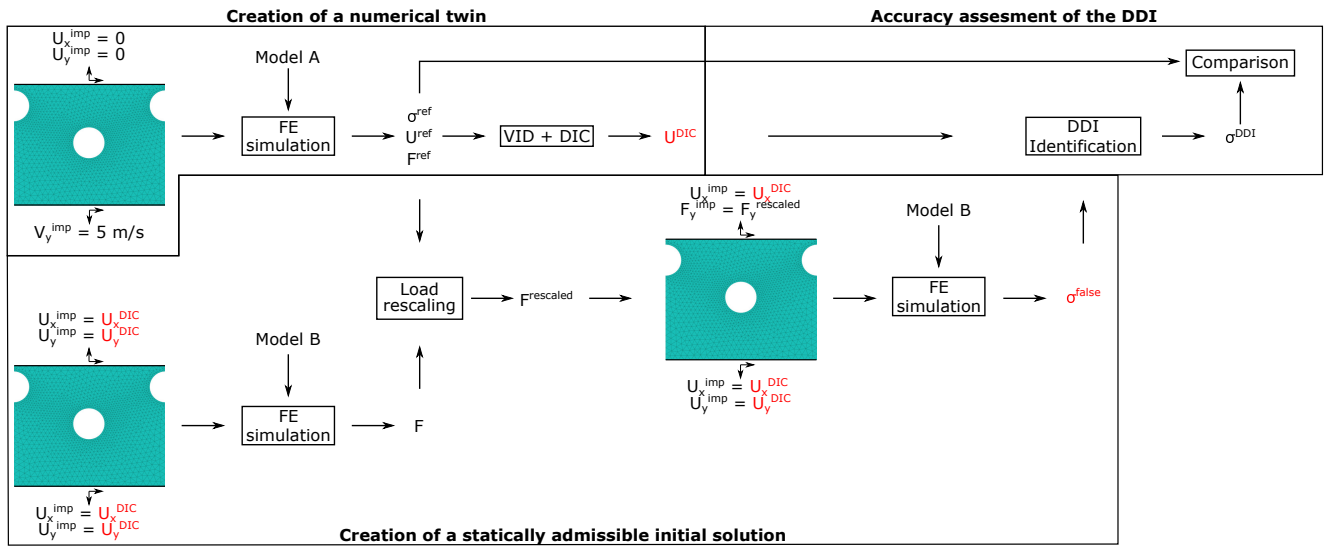


**FIGURE 9** Schematic of the numerical test case procedure. In red are the inputs of the *DDI* algorithm.

	$A$ (MPa)	$B$ (MPa)	$n$	$C$	$\dot{\epsilon}_0$ ( $s^{-1}$ )	$m$	$T_o$ (K)	$T_{melt}$ (K)
Model A	394 MPa	136 MPa	0.471	0.0259	$69.86 s^{-1}$	1.11	300	1350
Model B	315 MPa	272 MPa	0.6123	$2.56 \times 10^{-4}$	$69.86 s^{-1}$	1.11	300	1350

**TABLE 7** Parameters of the two Johnson-Cook model used for the FE simulations to assess the performances of the *DDI*.

is the most commonly used for the characterization of elasto-plastic behaviors. Figure 11a depicts the distribution of the identified mechanical points in this space. This figure shows the influence of the noise introduced in the VID procedure on the *DDI* results. Indeed, a main response is observed (characterized by mechanical states with high occurrence numbers) with a spread around it. This spread is especially important for strains beyond  $0.4 m m^{-1}$  as it reaches more than 150 MPa. Nevertheless, the occurrences of the mechanical states in the spread are several order of magnitude below the occurrences in the main response. Since the *DDI* method is data-based, it stands for a reason that the most recurrent mechanical states will lead to more robust identification. Indeed *DDI* relies on clustering method, hence robustness is strongly dependent on the density distribution of mechanical states in the constitutive space: database outliers, *e.g.* extreme localization (in space or time) can not be properly handled. In that context, the definition of *a posteriori* stress filtering method relying on mechanical state density seems relevant for eventually characterize the material. In what follows, a mechanical states is considered as relevant if its occurrence is higher than the 95<sup>th</sup> quantile. Figure 11b depicts the mechanical points distribution obtained after the proposed filtering. As expected, only the main response remains and the mechanical states spread is significantly reduced. Note that when using this filtering, only

9 % of the mechanical points are disregarded. This supports the use of this filter since it improves significantly the *DDI* results while disregarding a minimal amount of data. In the rest of this document, all the results will be presented after the use of the introduced filter. Figure 11c shows for each spatial element the number of time it is selected in percentage. This figure shows that most of the elements are selected for all the time steps. Furthermore, it can be observed that the elements disregarded are located near the notches and the central hole.

### Accuracy assessment

In order to assess the accuracy of the method and its ability to retrieve the reference stresses, the *DDI* stresses will be compared to them. To be as thorough as possible, the stress errors will be analyzed using different representations.

First, let us consider the stress uncertainty (that is to say the standard deviation of  $\Delta\sigma^i(e, t)$ ) achieved with respect to the stress magnitude. To this effect, Figure 12 depicts the stress magnitude distribution as well as the stress uncertainty (relative in blue and absolute in red) with respect to the stress magnitude. The distribution indicates that a significant amount of material points (space and time) are subjected to stress magnitudes below 200 MPa. This corresponds to the elastic domain of the considered material (see Fig. 11b). The higher stress identification errors in these regions, 100 % for low strains down to 12 % at 200 MPa, evidence that signal to noise ratio



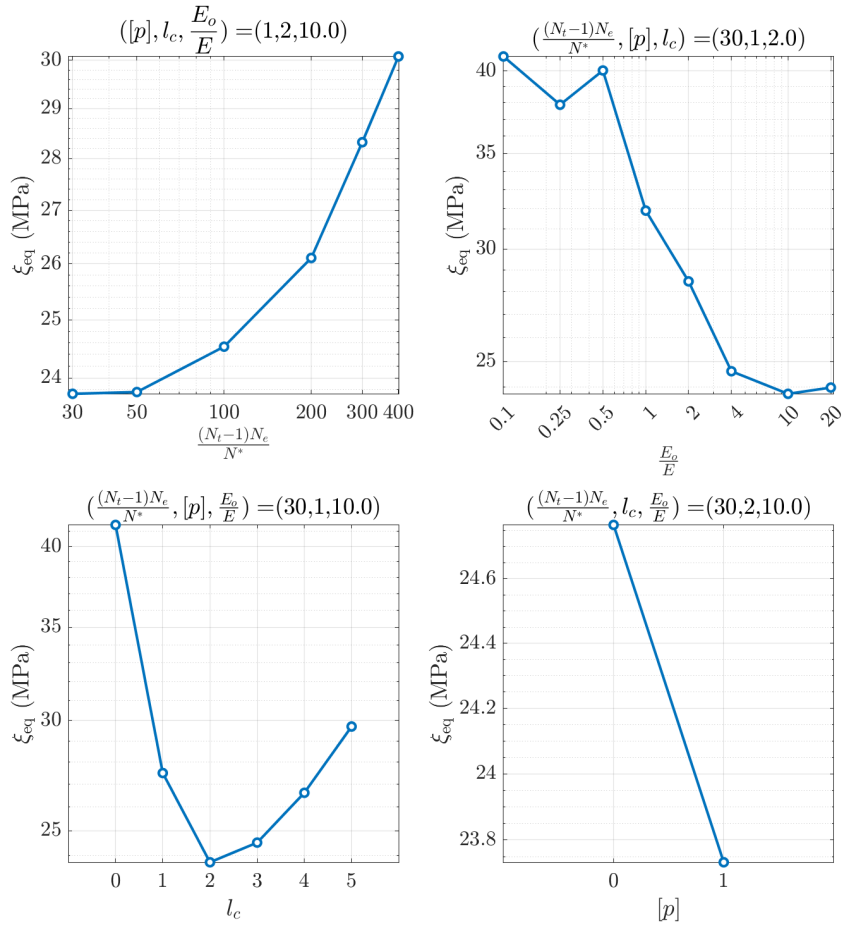


**FIGURE 10** Evolution of  $\xi_{\text{eq}}$  with respect to the DDI parameters. Note that the y-scale differs from one graph to another.

is here not favorable for identification. In addition, less data is available during elasticity, *i.e.* in the 200 MPa – 400 MPa range. The impact of the data scarcity in this range can be observed with the absolute stress uncertainty. Indeed, as the data availability in this range decreases, the absolute stress uncertainty increases from 9 MPa at the beginning to 27 MPa at 315 MPa. Nevertheless, since the signal to noise ratio becomes favorable, the relative stress error remains below 10 % after a stress magnitude of 200 MPa. At last, more data is available beyond 400 MPa *i.e.* during plasticity. The figure shows that beyond this stress magnitude, the error remains below 16 MPa that is to say a relative error of 4 %. Notice that such results are camera, geometry and loading dependent and should be checked for every new configuration.

Let us now investigate the accuracy of the method in the physical space. Figure 13 depicts for each element of the mesh their relative systematic (*i.e.* bias) and random stress (*i.e.* uncertainty) errors over time. Relative systematic errors tell what is the average systematic identification bias for any locations

while the random errors inform by how much the errors vary from the mean over time. It can be observed that the elements above and below the central hole and the notches present the highest errors (both systematic and random). This is to be expected since these elements are nearly always in the elastic domain (with a stress magnitude lower than 200 MPa), thus the signal to noise ratio is not favourable. Moreover, this figure shows that the errors near the localization bands are lower than 10 % $\pm$ 5 %. This is to be expected since in these regions, plasticity occurs and high stress magnitudes are obtained.

Another space of interest is the  $\{||\varepsilon||_{VM}, ||\sigma||_{VM}\}$ . Figures 14a and 14b respectively depict the distribution of the filtered mechanical points in the considered space and the associated stress errors. These figures support the observations made when analyzing Figure 12. Indeed, the errors are lower for mechanical states that are highly redundant and when plasticity occurs. Under these circumstances, the errors are below 5 %. In addition, despite the amount of data available during

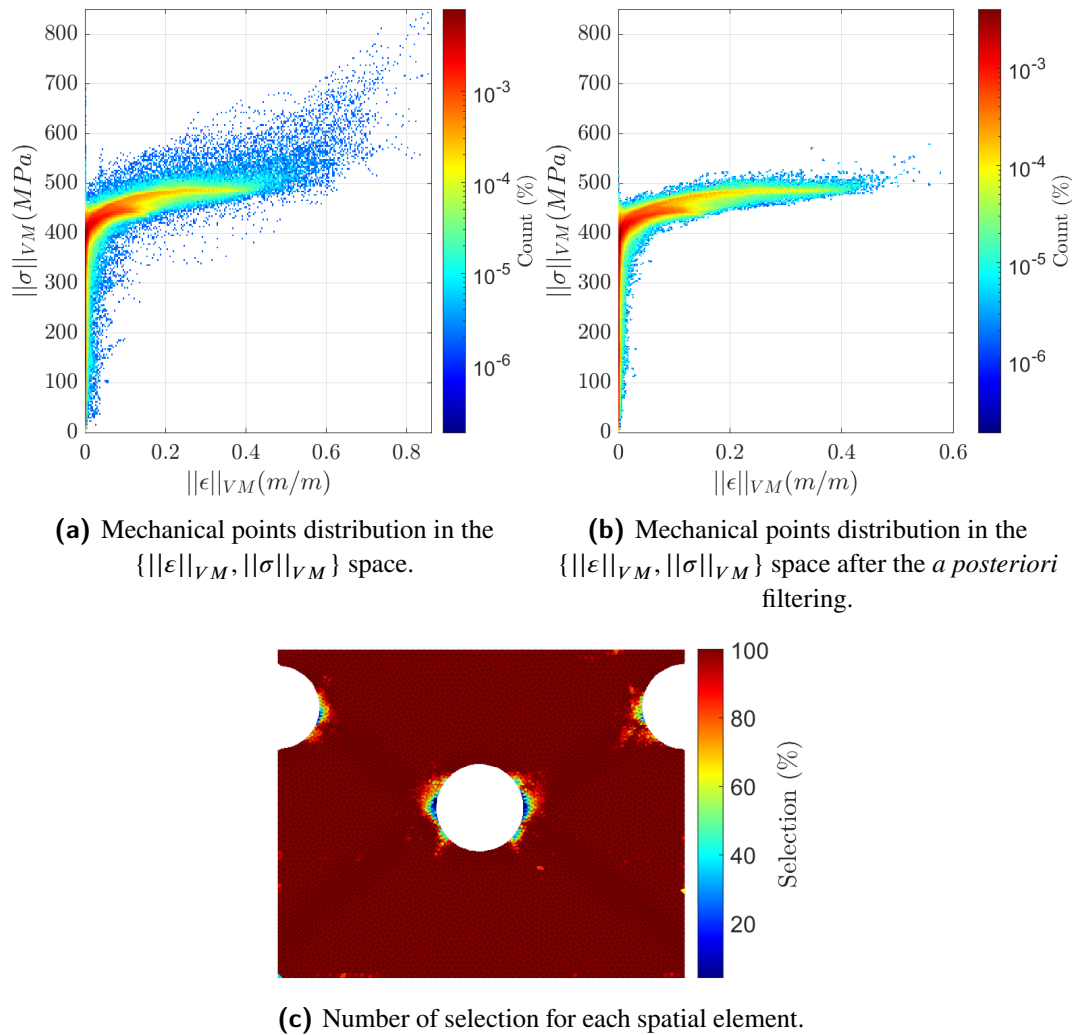


**FIGURE 11** Mechanical points distribution in the  $\{||\epsilon||_{VM}, ||\sigma||_{VM}\}$  space before and after the use of the filtering operator. The number of selection for each spatial element is also depicted in %.

elasticity, due to the unfavourable signal to noise ratio, high relative errors are obtained.

It is also of interest to consider the *DDI* relative error distribution in the  $\{I_1, \sqrt{3J_2}$  or  $||\sigma||_{VM}\}$  space. Indeed this space can be used to assess the triaxiality level reached by each material point at every time during the experiment. Figures 15a and 15b respectively depict the distribution of the filtered mechanical points in the considered space and the stress errors associated. The distribution shows that despite the introduction of a central hole and notches, most of the mechanical points are in a state close to uniaxial tension. Some uniaxial compression states are reached, but the stress amplitudes reached are not high enough to ensure a favorable signal to noise ratio. Thus, the stress errors remain higher than 20% for the points under uniaxial compression. Furthermore, this

figure shows that the mechanical points leading to the lowest error are obtained for the higher stress magnitudes (as already evidenced with the previous figures) and that these points are under mainly uniaxial tension. These observations are important since they evidence that whatever the complexity of the geometry, at least with such an heuristic design, multi-axiality and non-proportional loading would only be densely introduced within the sample using additional actuators. In the present case, it could be shown that local principal stress directions significantly varies, *i.e.* useful for characterization of material anisotropy, nevertheless multi-axiality are only reached either by some outliers, close to boundaries, or for very small strains, close to noise floor. Sample design optimization for *DDI* achievement should take all these points into consideration.



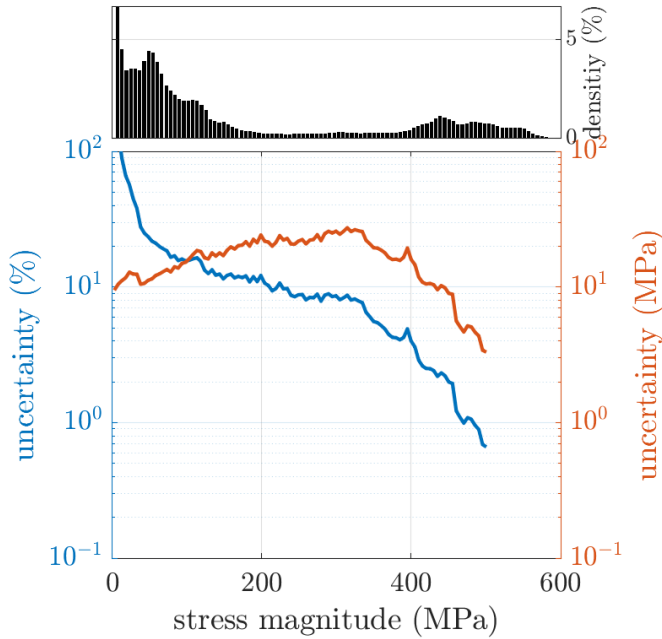


**FIGURE 12** Stress uncertainty with respect to the stress magnitude. The distribution of the stress magnitude is given by the histogram while the blue and red lines are respectively the relative and absolute values of the stress uncertainty. The values are obtained after the *a posteriori* filtering.

At last but not least, let us consider the *DDI* method ability to retrieve the strain-rate dependency of the reference stress fields. Indeed, let us recall that the stress fields used to initialize the method have a different strain-rate dependency than the sought ones. For this purpose averaged stress-strain curves, for material points undergoing similar mean strain-rates, can be plotted. To plot such a figure, the average strain-rate over time for each element is computed. Then, using a clustering algorithm (here k-means), these average strain-rates are regrouped in 20 clusters. The stress-strain curves are then obtained by averaging the stresses and strains for each cluster. Figure 16 then shows the relative errors at  $\|\epsilon\|_{VM} = 0.05, 0.10$  and  $0.15 \text{ mm}^{-1}$  for the 20 average strain-rates. The dashed lines depict the FE solution using model B (wrong initialization), while the stars depict the *DDI* converged solution. This figure confirms as expected that model A and the model B have different strain-rate dependencies. Indeed, the relative error of the initialization stress fields increases with the strain-rate for all the strain levels considered. Furthermore, this figure evidences that the *DDI* method is able to retrieve the sought strain-rate dependency even if the initial stress solution did not include it. This is supported by the fact that the relative error remains nearly constant below 6%, for all the strain levels considered. In short, even if the initialization does not truly capture the physics, *DDI* makes features of

the constitutive model, hidden within strain fields and load through equilibrium, naturally appear.

To summarize, by using kinematic fields from VID, one can assess the accuracy that can be obtained experimentally using the *DDI* method for the considered sample geometry, loading conditions and camera. The conclusions are as follows:

- Below 200 MPa the signal to ratio is not favourable, due to the noise on the strain measurements. The related mechanical points are mainly undergoing elastic strains. Furthermore these points are mainly located above and below the hole and notches.
- Since the method proposed is data-based, the abundance of data leads to low stress identification errors. Indeed, when data is sufficiently abundant errors remain below 5%.
- In the considered experiment most of the mechanical points are under a uniaxial tension state, despite the geometry considered. These points are located in the vicinity of the localization bands developing between the hole and the notches.
- At last, the *DDI* method is able to retrieve the correct strain-rate dependency of the reference within 6% of relative error. This illustrates the robustness of the method to its initialization and its ability to retrieve the features of the constitutive model.

## 5 | EXPERIMENTAL RESULTS AND DISCUSSIONS

This section finally discusses the database  $(\epsilon_i, \dot{\epsilon}_i, \sigma_i, T)$  with  $i \in \{1, 2, 6\}$  produced during the dynamic, uniaxial but heterogeneous test previously introduced. First, variation of macroscopic quantities are discussed, then kinematic fields. Eventually, identified stress fields are analysed and rate-dependencies of the material discussed in comparison with the parametric constitutive equation used at ONERA to classically model such a material, and are confronted to the data found in the literature.

### 5.1 | Evolution of macroscopic quantities during the test

The deconvolution between the distortions and the effective displacements is made following method presented in [41]). This allows the displacement, strain and strain-rate fields to be extracted. This allows the displacement, strain and strainrate

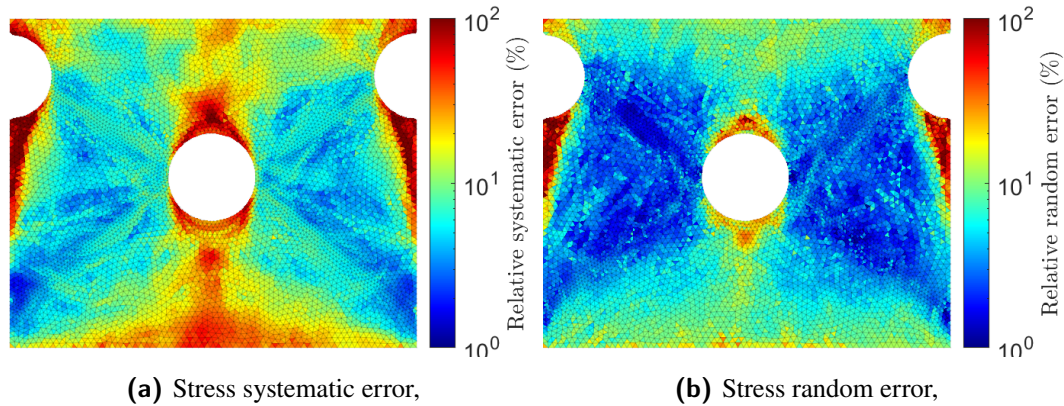


**FIGURE 13** Stress systematic and random error in the physical space. The values are obtained after the *a posteriori* filtering.

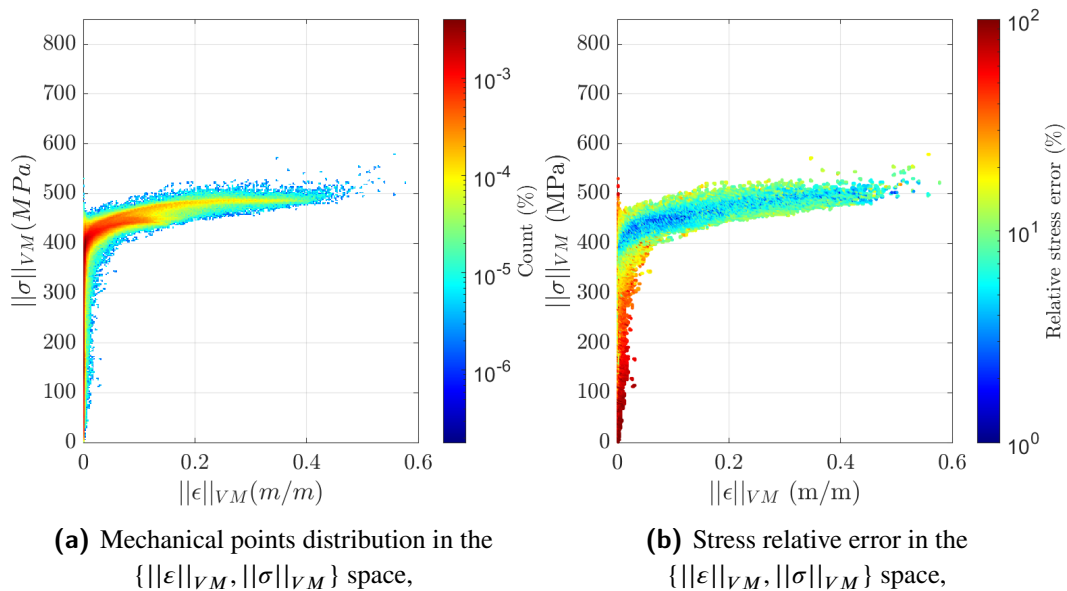
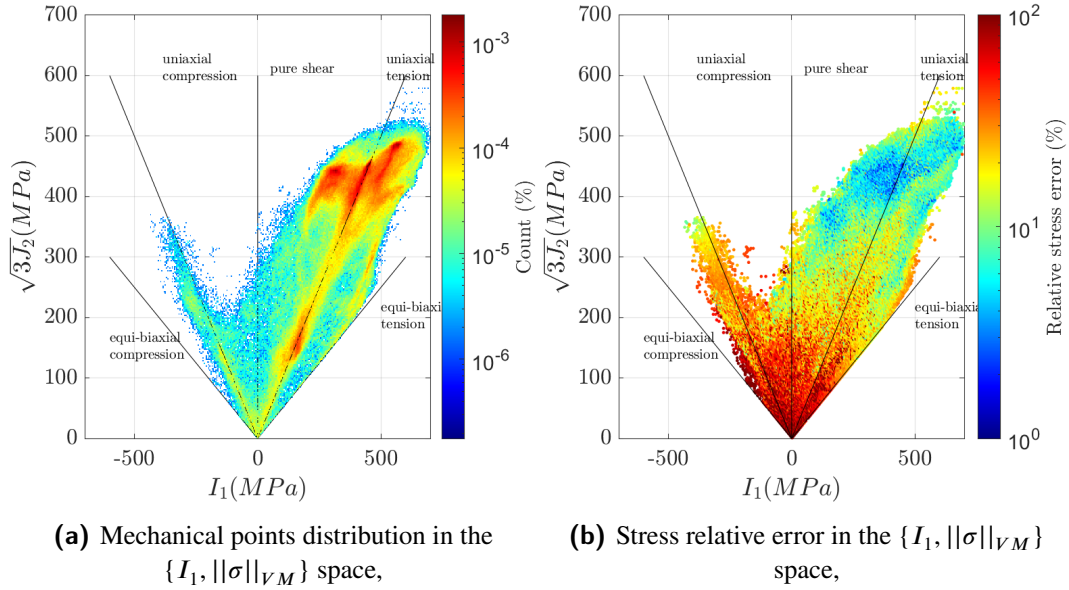


**FIGURE 14** Mechanical points distribution and stress relative errors obtained in the  $\{\|\epsilon\|_{VM}, \|\sigma\|_{VM}\}$  space after the *a posteriori* filtering.

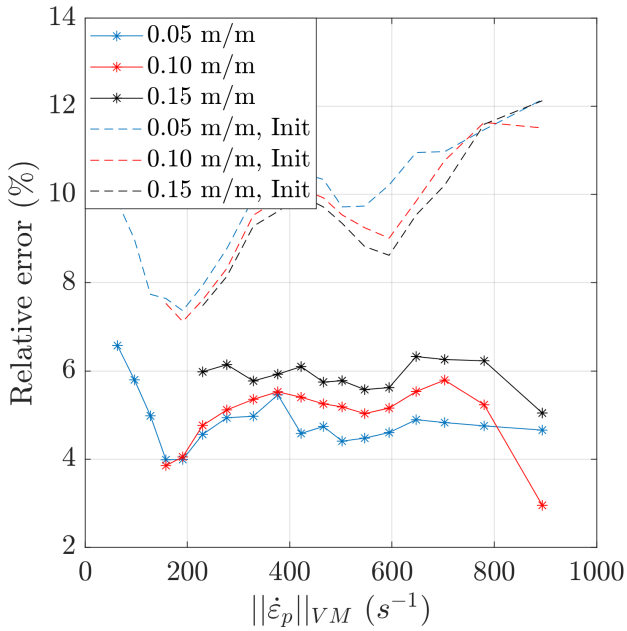
fields to be extracted.

Figure 17 depicts the evolution of different quantities of interest during the experiment. First, let us look at the temporal evolution of the averaged axial displacement and velocity of the nodes located at the bottom of the mesh, *i.e.* close to the sample head where the loading is applied. Figure 17a shows displacement in blue and velocity in red. The three vertical dashed lines are the time steps for which associated fields will be discussed later-on. Note that the zero in the timeline corresponds to the time when the Cordin-580 is triggered by the load cell, hence for the first images, negative times are obtained. The loading of the specimen induces immediately on the loaded

edge a displacement ramp, reaching about 2.8 mm before the initiation of sample failure. The velocities in the whole sample or for the nodes at the bottom of the mesh have the same trend. The velocities evidence two stages: from the beginning to approximately  $t = 370 \mu\text{s}$  the velocities increase in the tension direction, then from  $t = 370 \mu\text{s}$  to  $t = 620 \mu\text{s}$  they decrease. The second stage can be explained by considering the possibility that the contact between the sliding bar and its enclosing case is not permanent. Indeed, if the sample goes faster than the actuator, then when there is no more contact its speed will naturally decrease until there is contact again. One way to verify this hypothesis would have been to record accurately the speed of the actuator (using DIC with a high speed camera for



**FIGURE 15** Mechanical points distribution and stress relative errors obtained in the  $\{I_1, \|\sigma\|_{VM}\}$  space.



**FIGURE 16** Relative stress error evolution with respect to the strain-rate, computed for different strain levels. The stars represent the results obtained with the *DDI* while the dashed lines are those obtained with the FE initialization using model B.

instance). However, this was not done for these experiments. During the experiment, the maximum speed reached on the loaded edge is about  $4.8 \text{ m s}^{-1}$  in about  $476 \mu\text{s}$  which represents an acceleration on the order of  $10^4 \text{ s}^{-1}$ .

Figure 17b plots the evolution of the Von-Mises norm of both the total strain (in blue) and total strain-rates (in red) in a localization band during the experiment. This figure shows that during the first  $100 \mu\text{s}$  of the experiment, the sample is mainly in an elastic regime ( $\|\epsilon_t\|_{VM} \leq 0.005$ ). Furthermore, the total strain in the localization band becomes higher than 0.01 after about  $150 \mu\text{s}$ , after which it increases following a ramp until about  $0.22$  before the crack initiation. In the considered band, two stages of the normalized total strain-rate evolution can be observed. First, it ramps up to  $375 \text{ s}^{-1}$  in about  $300 \mu\text{s}$ . Then, the normalized total strain-rate reaches a plateau and oscillates between  $350 \text{ s}^{-1}$  and  $400 \text{ s}^{-1}$ . At last, Figure 17c shows the evolution of the load during the experiment (in blue). It also depicts – for information purpose only – the average temperature increase (in red) in the considered band. Two stages can be evidenced for the load. During the first  $150 \mu\text{s}$  the load ramps up until  $8 \text{ kN}$ . Then it reaches a plateau and oscillates around  $8.5 \text{ kN}$ . Considering an initial cross section  $S_0$  equal to  $1.68 \times 10^{-5} \text{ m}^2$  (subtracting the holes), the engineering stress can be estimated at  $500 \text{ MPa}$ . This value is in line with the ones obtained in [14].

A slight increase of temperature of about  $0.3 \text{ }^\circ\text{C}$  is observed while the sample should slightly cool down by the same amount due to thermoelasticity. This observation is explained by the uncertainty of approximately  $300 \text{ mK}$  achieved with the dedicated calibration procedure applied to retrieve temperature fields. This is already in the same order of magnitude as thermoelastic effects. Nevertheless, after  $100 \mu\text{s}$ , the temperature increases following the same trend as the normalized total strains, as expected. The sample temperature increase reaches

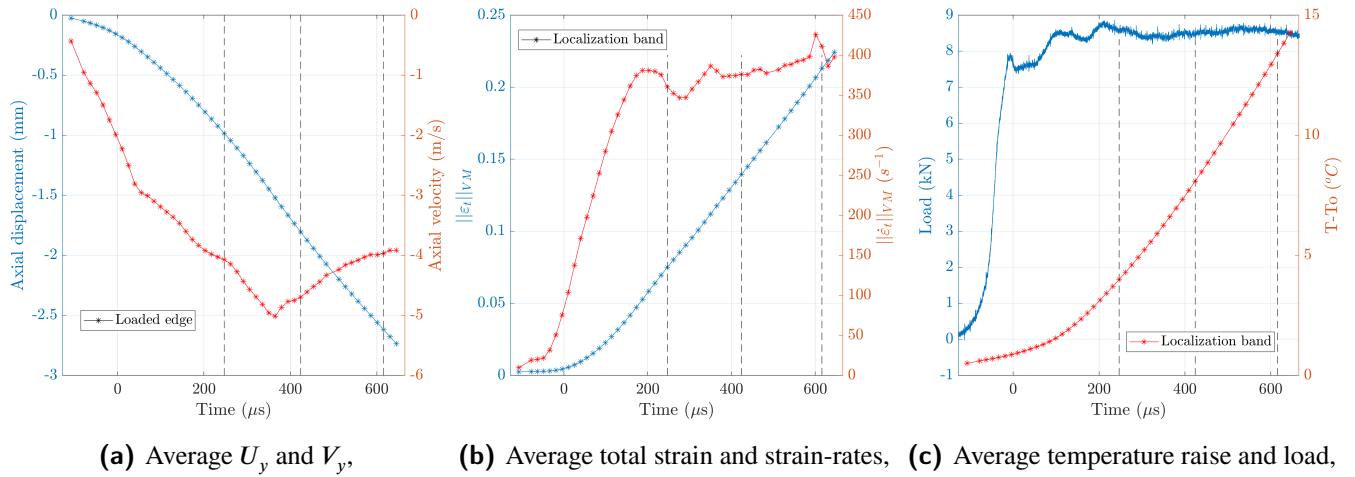


**FIGURE 17** Evolution of different quantities of interest during the test (either the loaded edge or in the localization band).

15 °C on average in the localization band before crack initiation with a rate on the order of 25 K/ms.

## 5.2 | Displacement and strain fields

Figure 18 shows the last raw image obtained during the high speed tensile test. In this image two cracks can be seen. On the left hand side there is a crack going from the central hole to the notch. On the right hand side, the crack only started to initiate from the central hole. In what follows, the analysis is performed on the images prior to the apparition of these cracks.

Figure 19 shows sample images, displacement fields in both directions, and the axial strain fields for the three time steps

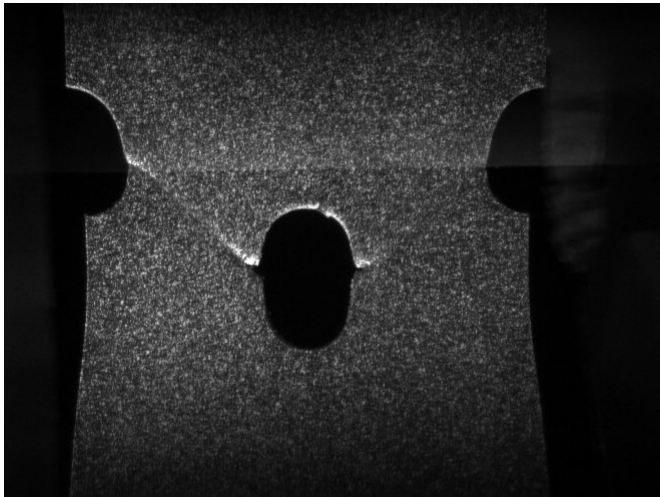


**FIGURE 18** Last raw image of the sample obtained during the test.

introduced previously. The displacement fields obtained are consistent with a tensile test. The first two images underline the fact that the tensile test is not perfectly axial. Indeed, the axial displacements are higher on the left-hand side of the sample. This phenomenon was observed for all the experiments performed as well as on the preliminary tests. In turn, crack initiation systematically begins on the left-hand side of the sample before the right-hand side. No clear explanations have been found for this observation. It may be partly due to the fact that the sample is already pre-constrained, and a non-planar contact between the sliding bar and its enclosing case may also come into play. However, no clear evidences have been found to confirm these hypotheses. The strain fields at 246.79 μs further confirm the fact that the load imposed on the sample is not symmetrical since strains are higher in the left band. The sample geometry induces localization bands as predicted by the FE simulations with little strain everywhere else.

In addition, strain and strain-rate ranges experienced by the sample during the test is investigated. To this effect, Figure 20 depicts the strain *versus* strain-rate (in Von-Mises norm) occurrences that are observed through the chosen ROI during the whole test. White areas represent states that the sample never reached. This figure shows that most of the sample during the experiment undergoes relatively small strains (below 0.05 m m<sup>-1</sup>), while a reasonable amount reaches 0.20 m m<sup>-1</sup>, as well as strain-rates varying mainly between 10 and 400 s<sup>-1</sup> with a huge predominance of strain-rates lower than 200 s<sup>-1</sup>. This is consistent with the strain fields obtained. Furthermore, let us note that before cracking, only a few points reach a total strain higher than 0.25 m m<sup>-1</sup>. Strain and strain-rates ranges of respectively [0 m m<sup>-1</sup> – 0.20 m m<sup>-1</sup>] and [0 s<sup>-1</sup> – 400 s<sup>-1</sup>] are in line with the one involved in the numerical twin.



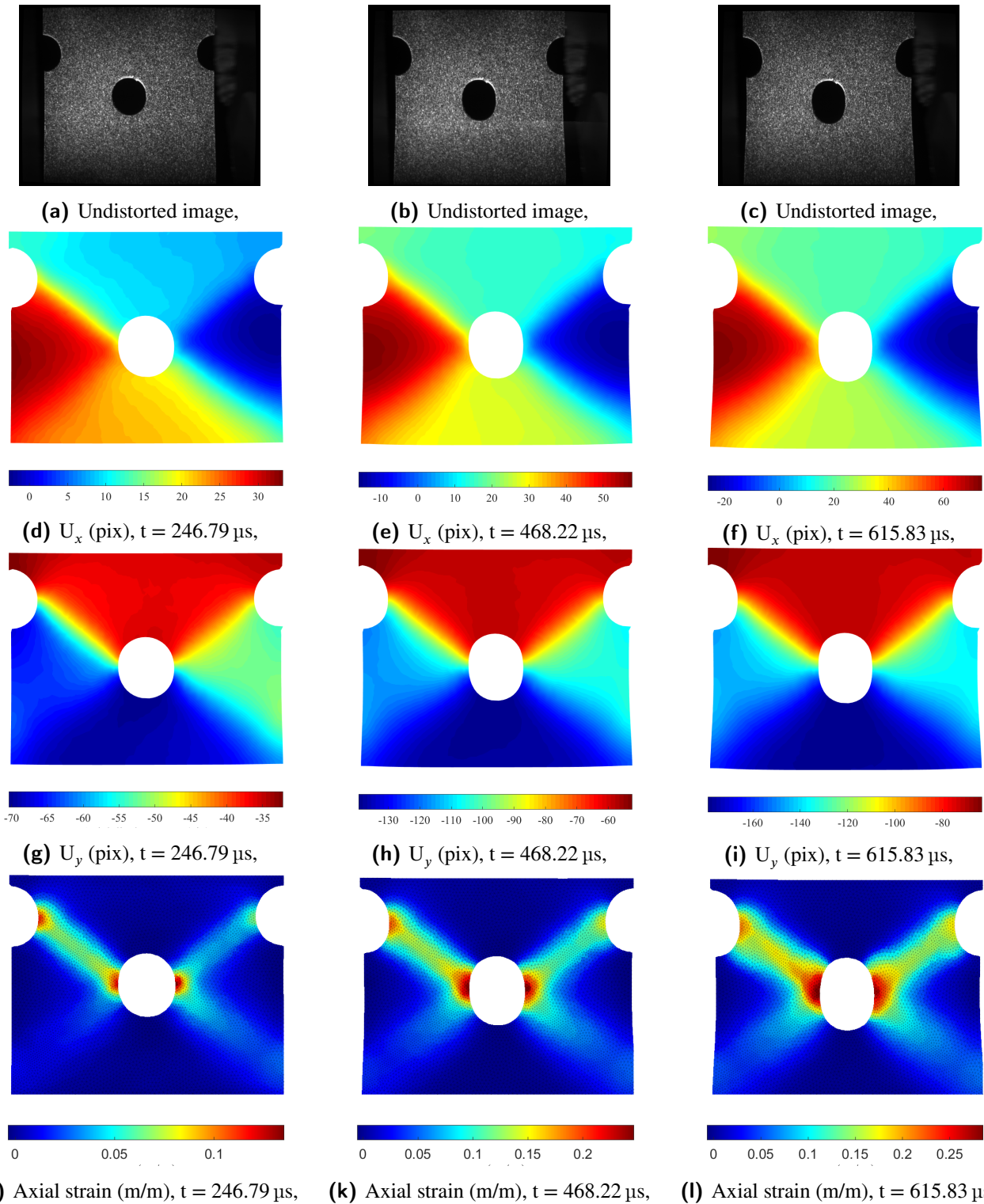


**FIGURE 19** Undistorted images, displacement fields, strain fields obtained during a dynamic tensile test, for different time steps.

### 5.3 | DDI experimental application to the XES characterization campaign

#### Stress fields

The *DDI* algorithm has been presented and then applied to a numerical test case in the previous section. Now the proposed method is applied to the data obtained during the XES

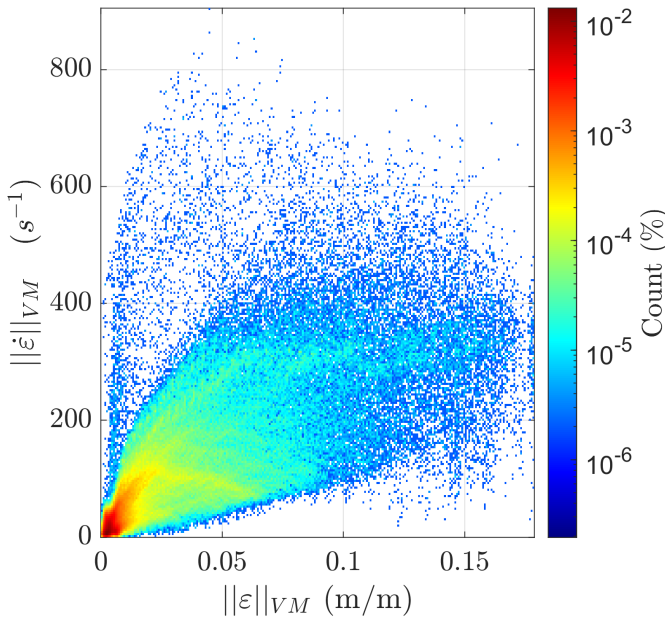


**FIGURE 20** Von-Mises norm of the strain vs Von-Mises norm of the strain-rates distribution obtained during the experiment, prior to crack initiation. The colour corresponds to a 2D histogram plot. The count per bin is normalized by the number of elements in the ROI times by the number of time steps. The strain states that were never experienced by the sample remain white.

characterization campaign. The performance of the proposed methodology will be discussed as well as its intrinsic limitations, of the material as well as the geometry chosen.

The experimental procedure for the *DDI* is very similar to the one presented in Fig. 9. In this case, the experimental data replace the ones obtained from the reference simulation of the numerical test case. As the *DDI* requires two FE simulations to be performed, the material model chosen for the initialization is the Johnson-Cook model and the parameters used are the one identified on the raw data from ONERA [29] (*i.e.* the model A from the numerical test case). Furthermore, the load that will be used to rescale the load profile is the one captured by the load cell during the dynamic tensile test adjusted following the method presented in Section 3. At last, the method's parameters are the ones considered optimal from the numerical twin study, *i.e.*  $N^* = 30$ ,  $E_o = 10.0 \cdot E$ ,  $l_c = 2$  and  $[p] = [w]$ . Additionally, the same *a posteriori* filtering operator will be applied on the results. Hence, all the results presented in what follows are obtained using these parameters and the *a posteriori* filter defined in Section 4. Notice that the mild-steel XES used in this study exhibits a complex strain-rate dependency that the classical multiplicative Johnson-Cook model can not capture.

In particular, this model fails to describe the uncoupled dependencies of the initial yield stress and the hardening modulus (see [40] for parametric study). In this context, the initialization is quite far from the expected measurements, probably even farther in the example considered in the numerical validation where same Johnson-Cook model were used but with different parameters.

Once the *DDI* algorithm applied, the mechanical and material states are available. From these states the Von-Mises norm of the stresses can be computed. Figure 21 depicts the spatial cartographies of respectively the total strains (pre-filtered with  $l_c = 2$ ) and the Von-Mises stresses for three different time steps. The cartography of the Von-Mises stresses (Fig. 21) shows that, as expected, the notches and the central hole create stress concentration bands. In these bands the Von-Mises stresses reach eventually about 500 MPa. In addition, in the secondary bands (*i.e.* pointing down), the stress is about 400 MPa. Above and below the central hole and the notches the stress magnitudes remain below 200 MPa. These observations are consistent with the numerical study performed. Figure 21a also confirms that the test is slightly non-symmetrical since the left localization (where the crack eventually forms) arises first.

Let us recall that the experiment was designed to provide different loading paths of the material and wide spectra of strain and strain-rates during a single test. Hence, Figure 22 enables the verification of these specifications. Figure 22a depicts the stress distribution in the space ( $I_1$ ,  $\sqrt{3}J_2$  or  $\|\sigma\|_{VM}$ ) for the selected mechanical states. It follows that this figure is an indicator of the stress triaxiality that occurs during the experiment. This figure shows that the sample is mainly under an uniaxial tensile state. However, some compression and shear states are reached within the specimen. In addition, Figure 22b shows that the strain and strain-rate spectra mainly seen by the specimen are  $[0 - 0.18]$  and  $[0 \text{ s}^{-1} - 450 \text{ s}^{-1}]$ . Nevertheless, some regions of the sample reach higher strain and higher strain rate values. In order to associate these states to a region in the sample, several elements located at different regions of interest of the sample are selected (see Fig. 22c). The loading paths of these elements are depicted in Fig. 22a and 22b superimposing markers with same color code. As it can be expected, the region above and below the hole (and by extension the notches) are under a compression state. Moreover, as expected, the elements in the band are mainly in a uniaxial tensile state. Figure 22b clearly highlights that the different regions of the bands are under different but quasi-constant strain-rates, at least during plastic regime. This further justifies the specimen geometry since it clearly demonstrates that at least the results of uniaxial tensile tests performed at different strain-rates can be retrieved. Nevertheless, this figure emphasizes a complexity inherent to all dynamic tests (even iso-static):

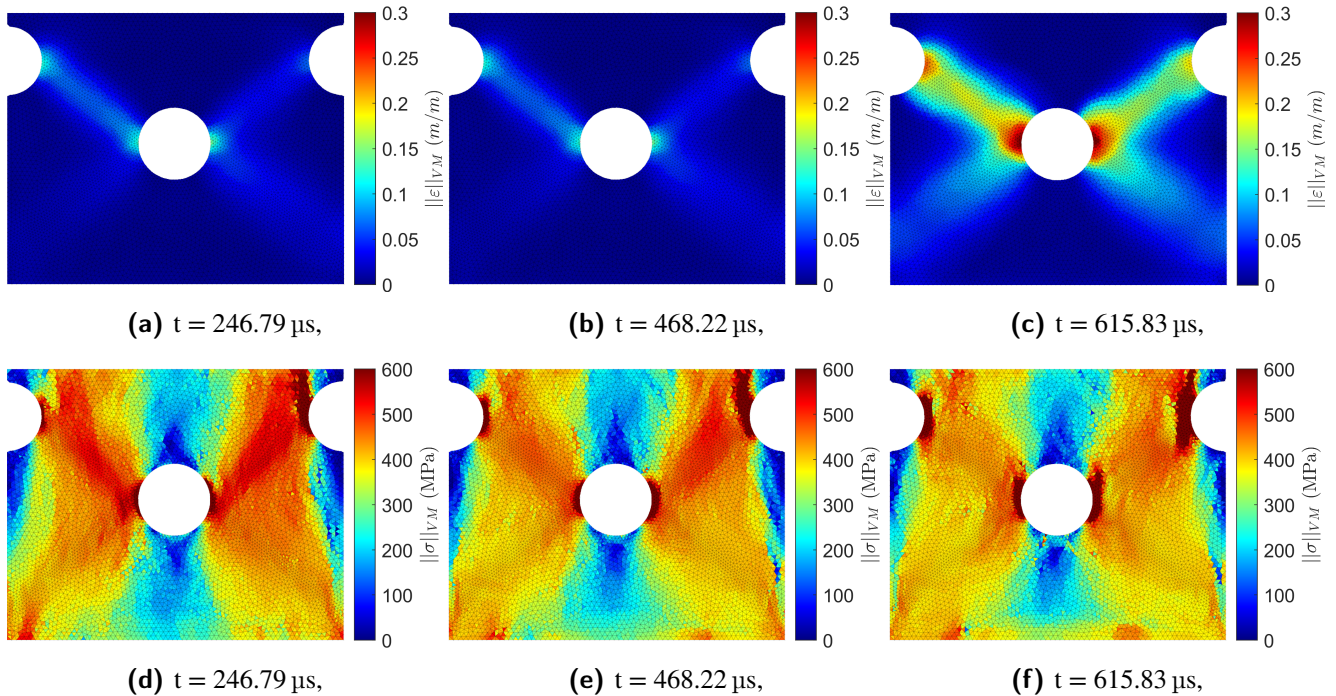


**FIGURE 21** Cartographies of the Von-Mises norm of the total strains and stresses for three different time steps.

material points in the elastic regime, in the elasto-plastic transition, then in stabilized plastic regime do not necessarily undergo similar strain-rates. Analysing this test in a mono-parametric way, *i.e.* considering an average strain-rate may be inaccurate since Young-modulus, yield-stress and flow hardening are actually not characterized in similar rate conditions. Grabbing high-dimension database from such tests may help to get the right data at the right conditions. This question goes way beyond the scope of this paper, nevertheless the question of rate-dependency characterization will slightly be discussed in the next section.

### Material behaviour of the XES steel: comparison with the reference data

As presented in Section 2, the material states average the mechanical response of the material and sample an underlying constitutive equation, within the chosen constitutive space. Furthermore, in order to take into account the *a posteriori* filtering introduced, only the material states associated to the selected mechanical states will be considered. In this paragraph, these material states will be compared to the two different set of data available at ONERA:

1. Reference data from [29], which consist in three stress-strain curves from tensile tests at  $0.006 \text{ s}^{-1}$ ,  $0.7 \text{ s}^{-1}$  and  $70 \text{ s}^{-1}$ . In their work the authors also identified parameters for the modified Krupkowsky model.

2. Reference data from [14], which consist in three stress-strain curves obtained with modified Hopkinson bars at  $200 \text{ s}^{-1}$ ,  $360 \text{ s}^{-1}$  and  $440 \text{ s}^{-1}$ .

Figure 23a depicts a projection of the material states within the Von-Mises stress-strain space. The black and red lines are the raw data from previous characterization of the XES steel performed at ONERA at different speeds. Notice that the observed spread has two origins:

1. The uncertainty of the method. Indeed, even after the *a posteriori* filtering (calibrated on numerical twin), some material states with singular behaviours are remaining.
2. The second is rate-dependency which appears as a spread in this projected sub-space.

As previously mentioned, temperature-dependence could induce an additional spread nevertheless, temperature variation induced in this test only by plastic dissipation remains too low to have any influence on the stress. Interestingly, the behaviour of the material at  $70 \text{ s}^{-1}$  obtained from previous characterization is well captured by the main trend of the *DDI* cloud of points. This is in line with the fact that the material considered in this study, known to be strain-rate dependent, has a dependency which fades at about  $100 \text{ s}^{-1}$  as it was observed in [14] where dedicated apparatus has been developed to probe the material response in tension from 200 to  $440 \text{ s}^{-1}$ .

To evidence that the spread observed in Fig. 23a results in first order from the rate-dependency of the material captured



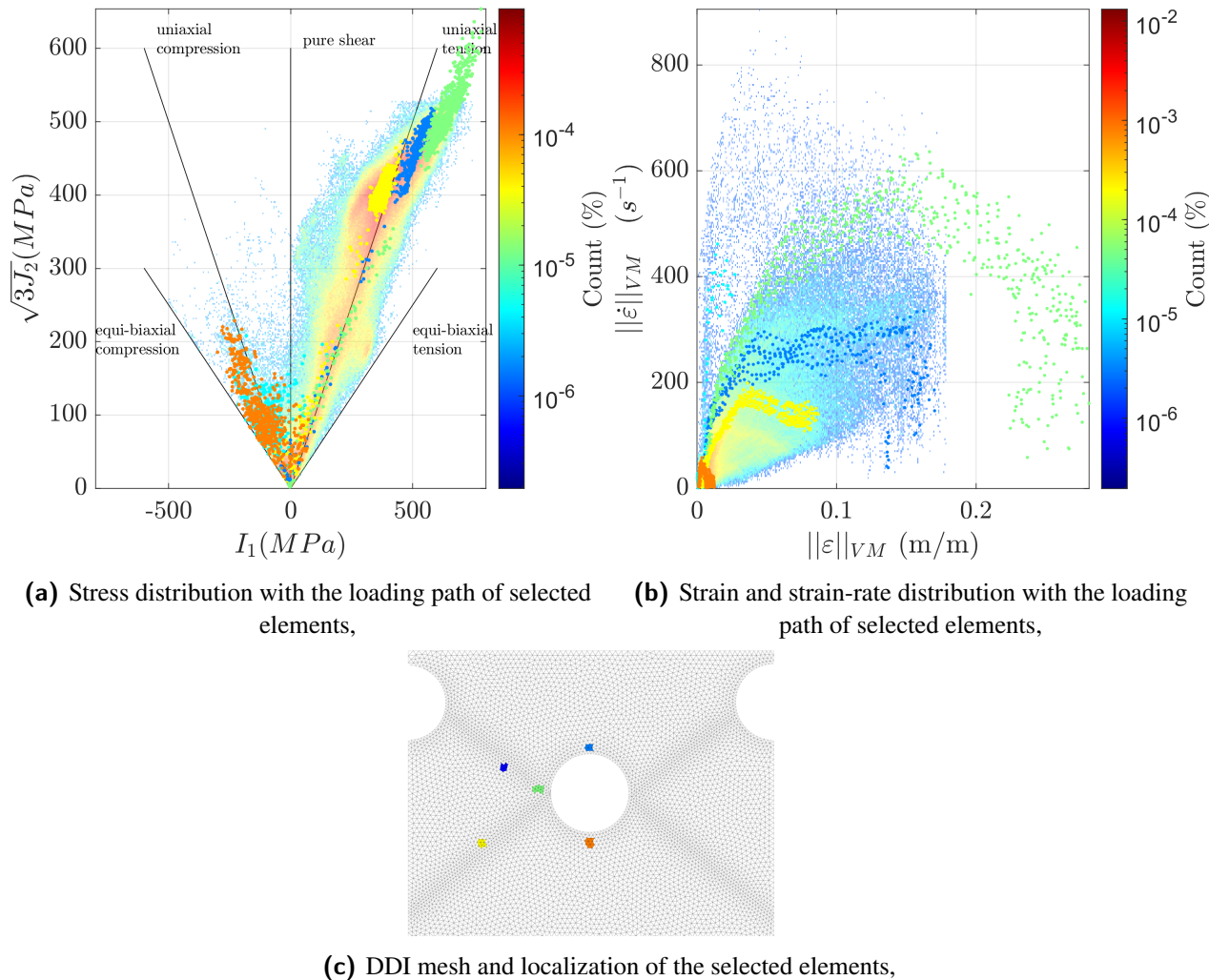
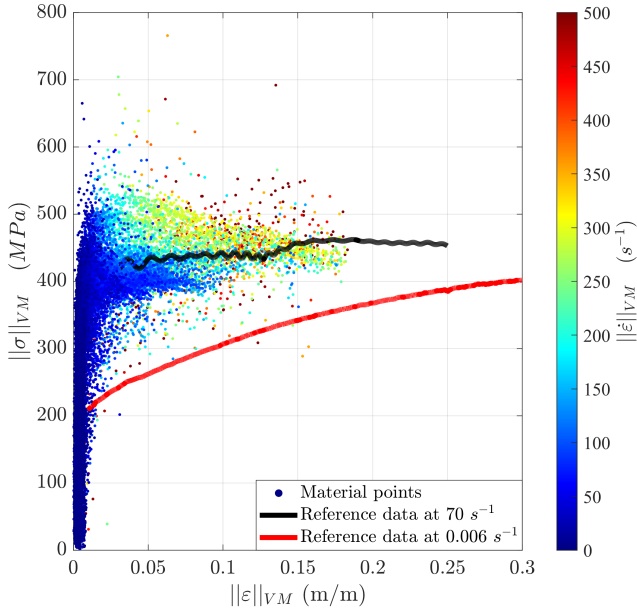


**FIGURE 22** Stress, strain and strain-rate distributions in  $(I_1, \sqrt{3J_2})$  or  $(\|\sigma\|_{VM})$  and  $(\|\epsilon\|_{VM}, \|\dot{\epsilon}\|_{VM})$  spaces, during the experiment for the selected mechanical states (i.e. not discarded by the mechanical state density filter). The loading paths of a few selected elements, presented in *c*, are superimposed on these distributions.

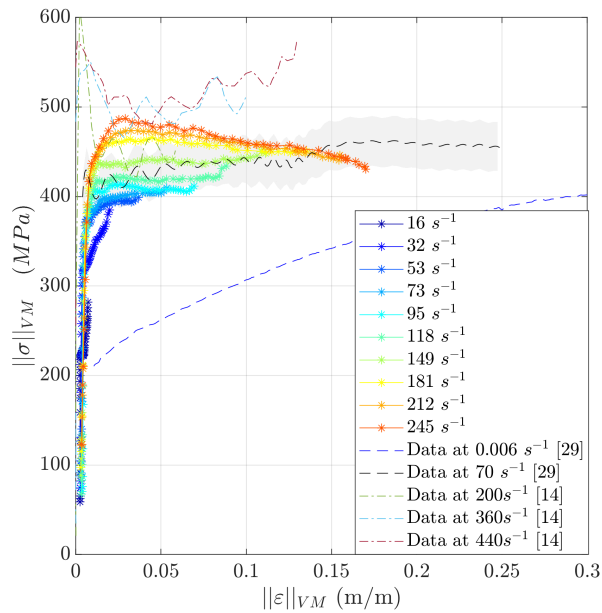
by the *DDI* approach, averaged stress-strain relations are also presented. Figure 23b shows 10 stress-strain curves computed by averaging states whose mean strain-rate over time are close as it was done for numerical twin (see Sec. 4.3). In addition, reference data from [29, 14] are. The grey area around the dashed line represents an uncertainty of  $\pm 6\%$ , in reference to the stress identification uncertainty found in the numerical validation for stresses above 400 MPa. This figure shows that the data obtained for an average strain-rate of  $81 \text{ s}^{-1}$  are in line with the reference data at  $70 \text{ s}^{-1}$  when taking into account the relative identification uncertainty. Data from  $80 \text{ s}^{-1}$  to  $191 \text{ s}^{-1}$  are also in line with the  $70 \text{ s}^{-1}$  reference data. In particular, the initial yield stresses as well as the hardening modulus obtained at these strain-rates seems well captured. The figure also confirms that the strain-rate dependency fades off around  $100 \text{ s}^{-1}$ ,

and the softening of the material response for strains below 0.05. Furthermore, this figure can be compared to the stress-strain curves obtained in the literature [14], that are depicted by dash-dotted lines. The *DDI* stress estimations are in line with the reference data from [29]. Indeed, we observe (using *DDI*) a decrease of the stresses for strain-rates higher than  $132 \text{ s}^{-1}$  with a stress peak near 500 MPa, while data obtained from [14] at  $200 \text{ s}^{-1}$ ,  $360 \text{ s}^{-1}$  and  $440 \text{ s}^{-1}$  show an increase of the peak stress up to 600 MPa followed by a softening. While the question of the reproducibility of the data using different experimental apparatus remains open, Figure 23b shows that *DDI* and a dedicated sample geometry allows to accurately capture, with a single apparatus, consistent elasto-plastic data from  $30 \text{ s}^{-1}$  to about  $250 \text{ s}^{-1}$ .





(a) Material states in  $(\|\epsilon\|_{VM}, \|\sigma\|_{VM})$ . The colour of the markers denote the strain-rates, while the lines denote the reference data from ONERA,



(b) Stress-strain curves for different averaged strain-rates extracted from the selected material states during one experiment,

**FIGURE 23** Material states in the space  $(\|\epsilon\|_{VM}, \|\sigma\|_{VM})$  as well as stress-strain curves for different averaged strain-rates obtained during one experiment.

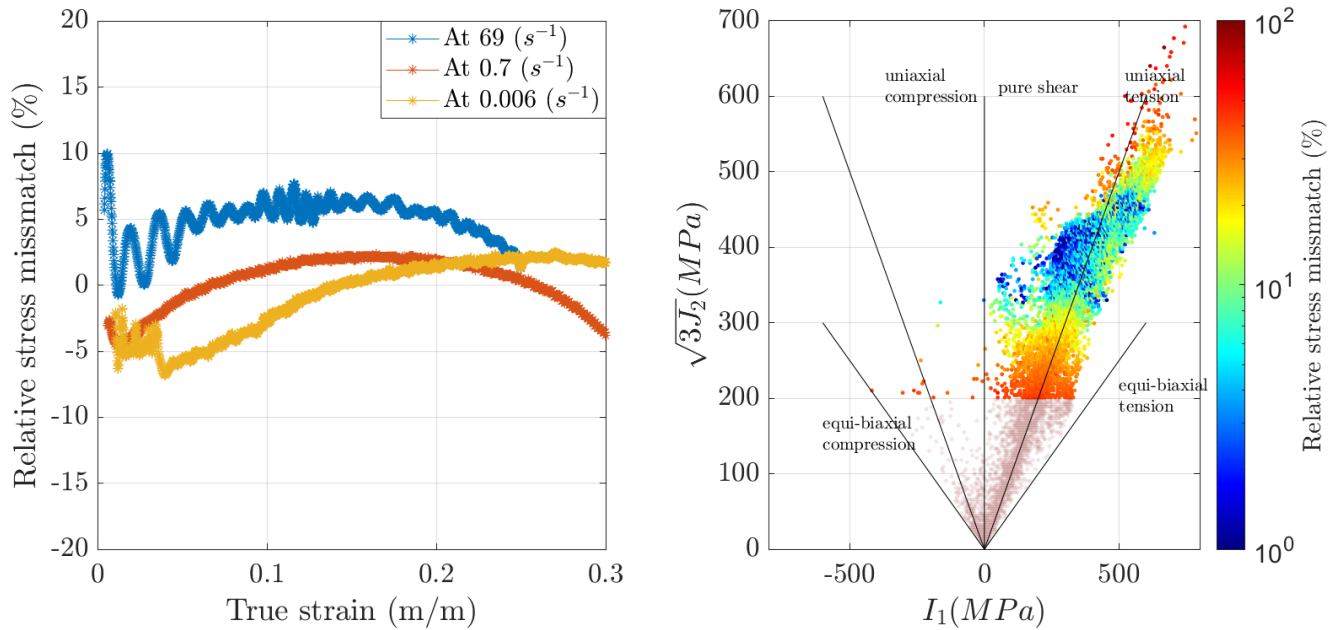
To go further, a dialogue between the material states and the modified Krupkowsky model can be made. On the one hand, the material states can be used in a conventional way to identify the whole set of modified Krupkowsky model constitutive parameters but from a single test. Then, the predicted stresses can be compared to the available experimental data from [29]. On the other hand, the comparison between the material states and the stresses predicted by the model using the parameters obtained from literature [29] can be performed. The idea is here to check how a model that is expected to fit well the non-linear strain-rate dependency of the XES steel compares itself to non-parametric material response identification beyond its experimental validity domain.

Hence, non-linear parameter identification is done using the Von-Mises norm of the *DDI* material states obtained as well as quasi-static data coming from [29], in order to ensure that the identified parameters characterize the material from quasi-statics to high strain-rates. The identification is performed for strains higher than 0.01. The parameters obtained are presented in Tab. 8, which also recalls the parameters from [29] coming from the compilation of multiple more standard tests. Strong variations are observed in particular for exponent  $c$  while  $\epsilon_0$ ,  $\dot{\epsilon}_0$  and  $b$ , which capture the strain-rate dependency, slightly differ from the reference parameters ( $\geq 15\%$ ). Finally,  $K$  and  $n$  are recovered within 3%. Despite these differences, predictions of the modified Krupkowsky model using updated parameters from *DDI* stresses are very close to Onera reference stress-strain curves [29]. Indeed, Fig 24a) shows that the reference data are captured within 6% for the quasi-static responses (0.006 and 0.7  $s^{-1}$ ) as well as for the intermediate strain-rate one (69  $s^{-1}$ ). This especially indicates that the model has a weak sensitivity to its parameters. Furthermore, its 7 parameters can be recovered from only 2 tests: a quasi-static one, and a high strain-rates heterogeneous one with *DDI*.

The material states obtained using this *DDI* method can also be compared to the stresses predicted by the modified Krupkowsky model, first with parameters obtained from literature [29]. The idea is here to check how a model that is expected to fit well the non-linear strain-rate dependency of the XES steel compares itself to non-parametric material response identification beyond its experimental validity domain. Hence, Figure 24b displays the cartography of the stress mismatch predicted by Krupkowsky and the material states in the stress invariant space. Since the modified Krupkowsky model describes the plastic flow, the data are compared for stress higher than 200 MPa. The cartography of the mismatch between the prediction using the modified Krupkowsky model and the *DDI* results in the stress invariant space is in quite good agreement with the one obtained in Section 4. Indeed, this figure shows that the *DDI* method is able to match

Parameters	$K$ (MPa)	$\epsilon_0$	$n$	$\dot{\epsilon}_0$ ( $s^{-1}$ )	$a$	$b$	$c$
Section 3	526.6	0.024	0.221	0.085	0.0002	0.385	0.002
This work + QS data	512.8	0.0281	0.2233	0.0705	0.0002	0.3361	0.0002
Relative variation (%)	2.62 %	-17.00 %	-1.04 %	17.04 %	0 %	12.71 %	90 %

**TABLE 8** Comparison of the modified Krupkowsky model parameters identified using data from [29] or from this work combined with quasi-static data from ONERA.



**(a)** Relative mismatch between reference data from ONERA [29] and prediction of the modified Krupkowsky model using the updated parameters identified from *DDI* stresses. **(b)** Comparison between the stress predictions using the modified Krupkowsky model and the material states from the *DDI*.

**FIGURE 24** Dialogue between the modified Krupkowsky model used at ONERA and the material states from the *DDI*.

the predictions from the constitutive model when the material is under uniaxial tension, within a relative discrepancy of about 5%. This comforts the fact that the modified Krupkowsky model, even calibrated over 3 uniaxial curves, is able to extrapolate well at higher strain-rates and when slightly deviated from its experimental validity domain. Nevertheless, notice that in the present case we don't know who is right, the prediction of the Krupkowsky model outside its experimental calibration domain or the *DDI* using heterogeneous test. Hence it is only possible to check where both agree or disagree and use the numerical twin uncertainty error for the interpretation.

To summarize, the *DDI* method has been applied to the experimental data obtained in Section 3. The stresses have been reconstructed. The stress distribution confirms that the

sample is mainly under uniaxial tension during the experiment, but some regions are under compression and shear (the region above and below the hole and notches for instance). The strain and strain-rate spectra that the sample is submitted to are  $[0 - 0.18]$  and  $[0 s^{-1} - 500 s^{-1}]$ . Furthermore, the *DDI* algorithm is able to retrieve the behaviour identified during previous characterization campaigns. In particular, using the material states obtained herein and data from a simple quasi-static test, constitutive parameters can be identified for the modified Krupkowsky model, which allows to retrieve the behaviour with a relative error below 10% for strain-rates from  $0.01 s^{-1}$  to a few hundreds of  $s^{-1}$ . At last but not least, based on the accuracy assessment performed in the previous section and a comparison with the predictions of the modified Krupkowsky model, this model's stress predictions can be considered with

confidence even when extrapolated for higher strain-rates than the ones used to calibrate it.

## 6 | CONCLUSIONS AND PERSPECTIVES

In this paper, an emerging inverse stress identification framework, named Data-Driven Identification, is presented and the recently developed rate-dependent formulation of the norm deployed for the first time to experimentally characterize material strain-rate dependence. Its accuracy has been assessed using a numerical twin. Then, a pre-notched sample with a central hole has been subjected to a high speed tensile test. Fullfield kinematic data have been obtained and quantitatively captured the events during the test. At last, these kinematic fields combined with load measurements have been used as input for the *DDI* method to estimate stress fields during the experiment. The main conclusions are as follows:

- The parameters of the *DDI* method play an important role in the stress reconstruction. A proper analysis performed on a numerical twin can rationalize the selection of these parameters.
- The numerical twin illustrates the ability of the proposed methodology to retrieve the material behaviour despite the use of a wrong set of constitutive parameters as initialization. It showed in particular that the algorithm is able to retrieve the material's strain-rate dependency accurately.
- Using the results from Virtual Image Deformation, the impact of noise on the stress estimation can be assessed. An accuracy of  $10\% \pm 5$  is obtained on the stress estimation. At last, using the *DDI* Data to perform parametric identification leads to relative errors lower than 5%. Such results are strongly dependent on the sample geometry, DIC parameters, camera and optics used. In this work, a multi-sensor Cordin-580 is considered. Such technology allows high spatial image resolution at ultra-high-speed at a cost of strong image distortions and sensor noise. In that context, presented experimental uncertainties much be seen as upper bounds and may be significantly reduced if new technologies for high spatial resolution ultra-high-speed imaging are developed in the market.
- The application of the proposed method to the experimental data allows estimating stress fields during non iso-static experiments. The material behaviour captured by the material states are consistent with the data obtained at ONERA during previous experimental campaigns compiling multiple uniaxial tensile tests at different loading rates. In the presented study, the stress are

retrieved with confidence for strains and strain-rates in the range of  $[0.01 - 0.18]$  and  $[10 \text{ s}^{-1} - 500 \text{ s}^{-1}]$  from a single test.

- Eventually, the complex non-linear, rate-dependence of the yield stress and hardening flow naturally appears from the data without having to write *a priori* the exact form of the constitutive equation contrary to standard parametric inverse methods. Only the framework, here rate-dependent is assumed within the form of the *DDI* norm.
- By combining the data from this work and data from a simple quasi-static test, constitutive parameters can be identified. These parameters are able to correctly retrieve the behaviour of the material over several strain-rates decades, with a relative mismatch that remains below 5 % compared to the data from [29].

*DDI* comes as a new brick within the experimentalist toolbox for both, local stress probing in the case of non-homogeneous loading case scenarios (*e.g.* local critical stress at fracture onset, flow stress during plastic instabilities, mechanical response of inclusions), and for material characterization. In the latter, as for more standard inverse methods, such as VFM or FEMU, *DDI* allows to make use of non iso-static configurations to characterize material behavior in a more efficient way but also over wider loading conditions domain. Its singularity relies in the fact that no *a priori* knowledge regarding the material constitutive equation is required which allows for not only identifying parameters but eventually the form of the constitutive equation itself in situations, especially dynamics, where strong couplings, instabilities, microstructural transformations make the constitutive equation unknown. We do believe, in a near future, that coupling topological optimization, DIC, *DDI* and deep-learning methods would allow for developing complex models, covering real case loading scenarios, in a record time.

## ACKNOWLEDGEMENTS

The support of Région Pays de la Loire, Nantes Métropole and European Union through grant Connect Talent IDS is gratefully acknowledged. The support of ANR through grant ANR-16-CE30-0007-01 is also gratefully acknowledged. Finally the authors would like to acknowledge all the colleagues and PhD students contributing to the informal working group, *Out-Law*, at GeM, especially Adrien Leygue and Raphael Langlois for the fruit-full discussions and their recent developments in rate-dependent *DDI*.



## APPENDIX

### A CORDIN-580

In this Appendix a brief recall of the operation of the Cordin-580 will be given. The readers can find more details in [41].

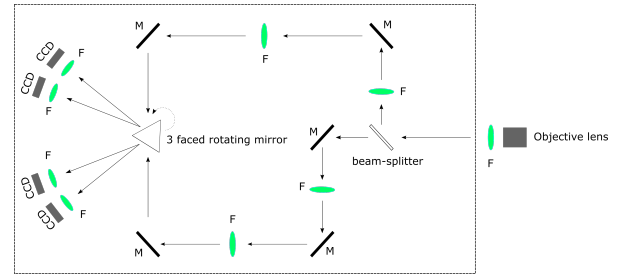
The camera used in this work is a Cordin-580. This camera is a rotating mirror camera that is able to capture 78 images with a resolution of  $2472 \times 3296$  pixels (i.e., 8 mega-pixels), up to a speed of 4 millions fps. For speeds below 500k fps, an electric turbine is used for mirror rotation. Between 500k fps and 1 million fps, a dedicated gas turbine is fed with compressed air. Finally, above 1 million fps, both the gas turbine and the camera must be fed with helium to increase the rotation speed and mitigate friction.

The optical apparatus used in the camera is depicted in Fig. A1a. The light-beam, depicted by the black arrows, enters the camera through the objective. It then encounters a cube beam-splitter, that will either transmit the light or reflect it with an angle of  $45^\circ$ . The light is then reflected on mirrors until it reaches a lens. After this lens, another mirror reflects the light beam onto a 3-faced rotating mirror. Finally, the light goes through a lens, used to mitigate the bias induced by the mirror rotation over individual sensor exposure time, and eventually reaches the sensor. Additionally, some specificities of the camera's geometry are worth mentioning. First, in order to let the light beams pass, Sensors 40 and 80 do not exist, thus black images are given for these theoretical sensors. Furthermore, due to their positioning, Sensors 21 to 60 are always the ones hit by the beam reflected by the beam-splitter. For the same geometrical reasons, Sensors 1, 39, 41 and 79 are illuminated when the rotating mirror is nearly perpendicular to the light beam. On the contrary, Sensors 20, 21, 60 and 61 are illuminated when the rotating mirror is hit by the beam with a shallow angle. This is illustrated in Fig. A1b.

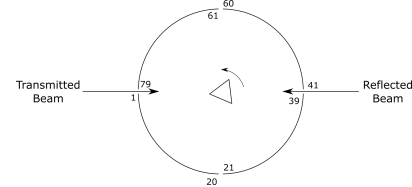
This complex optical apparatus leads to strong distortions on the raw images. Thus, in [41] a dedicated strategy to capture camera-induced distortions and then perform DIC has been developed and can be summarized as follows:

- A known reference image is needed in the procedure.
- There is a composition between the DIC displacements  $\underline{u}_{\text{DIC}}$ , the effective displacements  $\underline{u}_r$  and the distortions  $\underline{u}_d$ :  

$$\underline{u}_{\text{DIC}}(\underline{X}) = \underline{u}_r(\underline{X}) + \underline{u}_d(\underline{X} + \underline{u}_r(\underline{X})).$$
- The distortions are calibrated using a reduced basis of the Zernike polynomials.



(a) Schematic diagram of the Cordin-580 and its components: M, mirrors; L, lens; CCD, CCD sensors.



(b) Schematic diagram of the sensor layout.

FIGURE A1 Schematic diagram of the Cordin-580.

- Several acquisitions are performed on a static sample in the experimental setup in order to construct a statically representative model of the camera-induced distortions.
- The experimental kinematic data are retrieved by using the camera model to decompose the distortions of the effective displacements.
- The accuracy of the method is:
  - Displacements:  $0.5^{\pm 0.2}$  pixels.
  - Strains:  $0.1^{\pm 2}$  mm/m.

Figure A2 summarizes the procedure:

## References

- [1] Badaloni, M., M. Rossi, G. Chiappini, P. Lava, and D. Debruyne, 2015: Impact of experimental uncertainties on the identification of mechanical material properties using DIC. *Experimental Mechanics*, **55**, no. 8, 1411–1426, doi:10.1007/s11340-015-0039-8. URL <http://link.springer.com/10.1007/s11340-015-0039-8>
- [2] Barroqueiro, B., A. Andrade-Campos, J. D. de Oliveira, and R. Valente, 2020: Design of mechanical heterogeneous specimens using topology optimization. *International Journal of Mechanical Sciences*, **181**, 105764, doi:https://doi.org/10.1016/j.ijmecsci.2020.105764. URL <https://www.sciencedirect.com/science/article/pii/S0020740320305166>

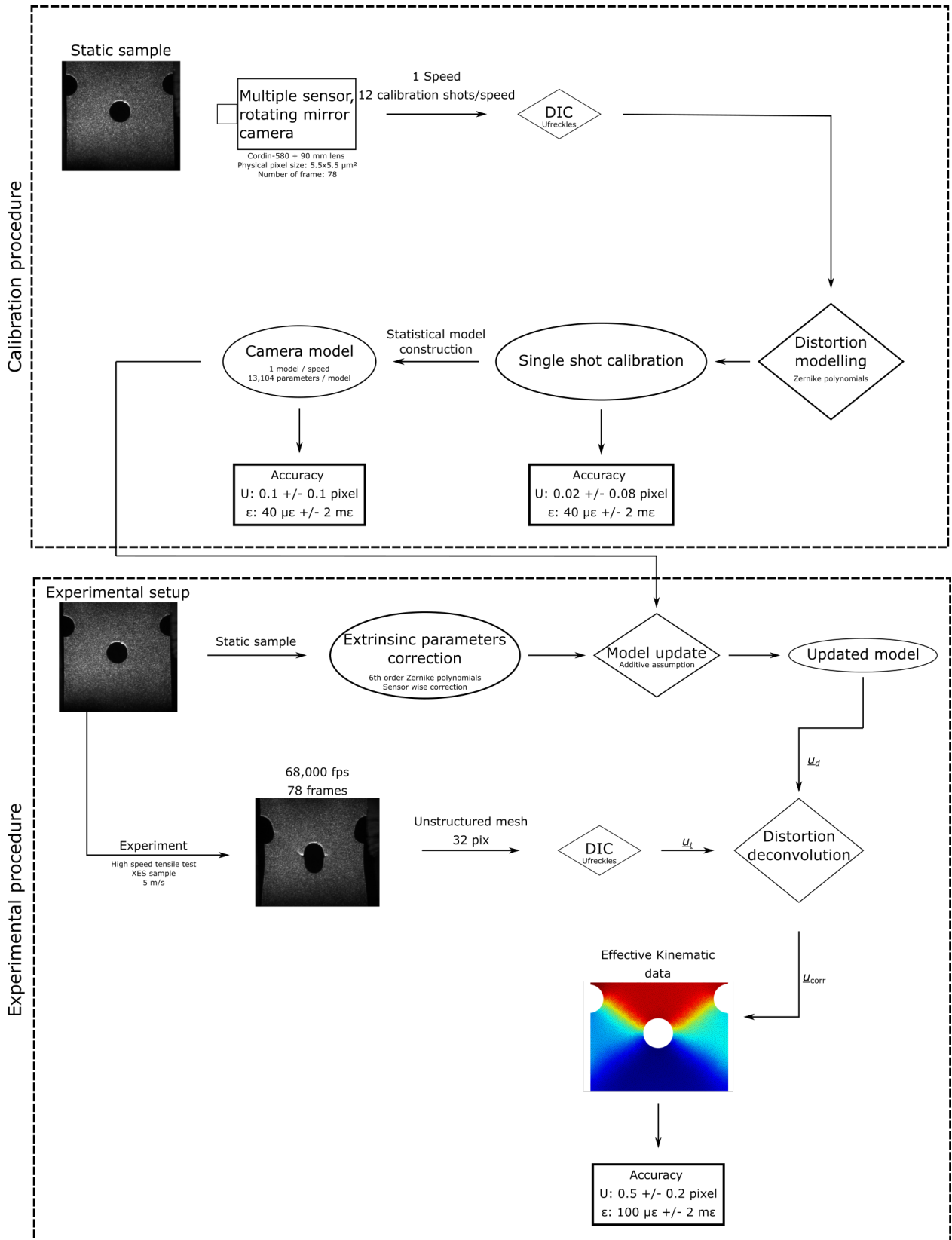


**FIGURE A2** Schematic representation of the calibration and experimental procedures used to obtain quantitative kinematic data using a Cordin-580.

- [3] Bouda, P., B. Langrand, D. Notta-Cuvier, E. Markiewicz, and F. Pierron, 2019: A computational approach to design new tests for viscoplasticity characterization at high strain-rates. *Computational Mechanics*, **64**, no. 6, 1639–1654, doi:10.1007/s00466-019-01742-y.  
URL <http://link.springer.com/10.1007/s00466-019-01742-y>
- [4] Cameron, B. C. and C. Tasan, 2021: Full-field stress computation from measured deformation fields: A hyperbolic formulation. *Journal of the Mechanics and Physics of Solids*, **147**, 104186, doi:10.1016/j.jmps.2020.104186.  
URL <https://linkinghub.elsevier.com/retrieve/pii/S0022509620304130>
- [5] Chamoin, L., C. Jailin, M. Diaz, and L. Quesada, 2020: Coupling between topology optimization and digital image correlation for the design of specimen dedicated to selected material parameters identification. *International Journal of Solids and Structures*, **193-194**, 270–286, doi:10.1016/j.ijsolstr.2020.02.032.  
URL <https://linkinghub.elsevier.com/retrieve/pii/S0020768320300792>
- [6] Dalémat, M., M. Coret, A. Leygue, and E. Verron, 2021: Robustness of the data-driven identification algorithm with incomplete input data, working paper or preprint.  
URL <https://hal.archives-ouvertes.fr/hal-03028848>
- [7] Dalémat, M., M. Coret, A. Leygue, and E. Verron, 2019: Measuring stress field without constitutive equation. *Mechanics of Materials*, **136**, 103087, doi:10.1016/j.mechmat.2019.103087.  
URL <https://linkinghub.elsevier.com/retrieve/pii/S0167663619302376>
- [8] Eggersmann, R., T. Kirchdoerfer, S. Reese, L. Stainier, and M. Ortiz, 2019: Model-Free Data-Driven inelasticity. *Computer Methods in Applied Mechanics and Engineering*, **350**, 81–99, doi:10.1016/j.cma.2019.02.016.  
URL <https://linkinghub.elsevier.com/retrieve/pii/S0045782519300878>
- [9] Fletcher, L., F. Davis, S. Dreuilhe, A. Marek, and F. Pierron, 2021: High strain rate elasto-plasticity identification using the image-based inertial impact (IBII) test part 1: Error quantification. *Strain*, **57**, no. 2, doi:10.1111/str.12375.  
URL <https://onlinelibrary.wiley.com/doi/10.1111/str.12375>
- [10] Fletcher, L. and F. Pierron, 2018: An image-based inertial impact (IBII) test for tungsten carbide cermets. *Journal of Dynamic Behavior of Materials*, **4**, no. 4, 481–504.
- [11] — 2020: The Image-Based Inertial Release (IBIR) Test: A New High Strain Rate Test for Stiffness Strain-Rate Sensitivity Identification. *Experimental Mechanics*, **60**, no. 4, 493–508, doi:10.1007/s11340-019-00580-6.  
URL <http://link.springer.com/10.1007/s11340-019-00580-6>
- [12] Fletcher, L., J. Van-Blitterswyk, and F. Pierron, 2019: A novel image-based inertial impact test (IBII) for the transverse properties of composites at high strain rates. *Journal of Dynamic Behavior of Materials*, **5**, no. 1, 65–92.
- [13] Gary, G. and W. K. Nowacki, 1994: Essai de cisaillement plan appliqué à des tôles minces. *Journal de Physique IV*, **04**, no. C8, C8–65–C8–70, doi:10.1051/jp4:1994809.  
URL <http://www.edpsciences.org/10.1051/jp4:1994809>
- [14] Haugou, G., E. Markiewicz, and J. Fabis, 2006: On the use of the non direct tensile loading on a classical split Hopkinson bar apparatus dedicated to sheet metal specimen characterisation. *International Journal of Impact Engineering*, **32**, no. 5, 778–798, doi:10.1016/j.ijimpeng.2005.07.015.  
URL <https://linkinghub.elsevier.com/retrieve/pii/S0734743X05001107>
- [15] Hollomon, J. H., 1945: Tensile deformation. *Aime Trans*, **12**, no. 4, 1–22.
- [16] Jones, E., J. Carroll, K. Karlson, S. Kramer, R. Lehoucq, P. Reu, and D. Turner, 2018: Parameter covariance and non-uniqueness in material model calibration using the Virtual Fields Method. *Computational Materials Science*, **152**, 268–290, doi:10.1016/j.commatsci.2018.05.037.  
URL <https://linkinghub.elsevier.com/retrieve/pii/S0927025618303501>
- [17] Kirchdoerfer, T. and M. Ortiz, 2016: Data-driven computational mechanics. *Computer Methods in Applied Mechanics and Engineering*, **304**, 81–101, doi:10.1016/j.cma.2016.02.001.  
URL <https://linkinghub.elsevier.com/retrieve/pii/S0045782516300238>
- [18] — 2017: Data Driven Computing with noisy material data sets. *Computer Methods in Applied Mechanics and Engineering*, **326**, 622–641, doi:10.1016/j.cma.2017.07.039.  
URL <https://linkinghub.elsevier.com/retrieve/pii/S0045782517304012>
- [19] — 2018: Data-driven computing in dynamics: Data-driven computing in dynamics. *International Journal*

- for *Numerical Methods in Engineering*, **113**, no. 11, 1697–1710, doi:10.1002/nme.5716.  
URL <https://onlinelibrary.wiley.com/doi/10.1002/nme.5716>
- [20] Klepaczko, J. R., H. V. Nguyen, and W. K. Nowacki, 1999: Quasi-static and dynamic shearing of sheet metals. *European Journal of Mechanics - A/Solids*, **18**, no. 2, 271–289, doi:10.1016/S0997-7538(99)80016-3.  
URL <https://linkinghub.elsevier.com/retrieve/pii/S0997753899800163>
- [21] Langlois, R., M. Coret, and J. Réthoré, 2022: Non-parametric stress field estimation for history-dependent materials: Application to ductile material exhibiting piobert–luders localization bands. *Strain*, e12410.
- [22] Langrand, B. and A. Combescure, 2004: Non-linear and failure behaviour of spotwelds: a “global” finite element and experiments in pure and mixed modes I/II. *International Journal of Solids and Structures*, **41**, no. 24-25, 6631–6646, doi:10.1016/j.ijsolstr.2004.06.009.  
URL <https://linkinghub.elsevier.com/retrieve/pii/S0020768304003245>
- [23] Langrand, B. and E. Markiewicz, 2010: Strain-rate dependence in spot welds: Non-linear behaviour and failure in pure and combined modes I/II. *International Journal of Impact Engineering*, **37**, no. 7, 792–805, doi:10.1016/j.ijimpeng.2010.01.004.  
URL <https://linkinghub.elsevier.com/retrieve/pii/S0734743X10000163>
- [24] LeBlanc, M. and D. Lassila, 1996: a hybrid technique for compression testing at intermediate strain rates. *Experimental Techniques*, **20**, no. 5, 21–24, doi:10.1111/j.1747-1567.1996.tb00459.x.  
URL <http://doi.wiley.com/10.1111/j.1747-1567.1996.tb00459.x>
- [25] Leygue, A., M. Coret, J. Réthoré, L. Stainier, and E. Veron, 2018: Data-based derivation of material response. *Computer Methods in Applied Mechanics and Engineering*, **331**, 184–196, doi:10.1016/j.cma.2017.11.013.  
URL <https://linkinghub.elsevier.com/retrieve/pii/S0045782517307156>
- [26] Leygue, A., R. Seghir, J. Réthoré, M. Coret, E. Veron, and L. Stainier, 2019: Non-parametric material state field extraction from full field measurements. *Computational Mechanics*, **64**, no. 2, 501–509, doi:10.1007/s00466-019-01725-z.  
URL <http://link.springer.com/10.1007/s00466-019-01725-z>
- [27] Liu, C., 2021: Nonuniform Stress Field Determination Based on Deformation Measurement. *Journal of Applied Mechanics*, **88**, no. 7, 071005, doi:10.1115/1.4050535.  
URL <https://asmedigitalcollection.asme.org/appliedmechanics/article/88/7/071005/1104370/Nonuniform-Stress-Field-Determination-Based-on>
- [28] MacQueen, J. et al., 1967: Some methods for classification and analysis of multivariate observations. *Proceedings of the fifth Berkeley symposium on mathematical statistics and probability*, Oakland, CA, USA, volume 1, 281–297.
- [29] Markiewicz, E., B. Langrand, N. Leconte, J. Fabis, and T. Dupuy, 2016: A methodology for the viscoplastic behaviour characterisation of spot-weld heat affected materials. *Journal of Materials Processing Technology*, **238**, 169–180, doi:10.1016/j.jmatprotec.2016.07.022.  
URL <https://linkinghub.elsevier.com/retrieve/pii/S0924013616302394>
- [30] Pierron, F. and L. Fletcher, 2019: Generalized stress–strain curves for IBII tests on isotropic and orthotropic materials. *Journal of Dynamic Behavior of Materials*, **5**, no. 2, 180–193, doi:10.1007/s40870-019-00197-9.  
URL <http://link.springer.com/10.1007/s40870-019-00197-9>
- [31] Pierron, F., H. Zhu, and C. Siviour, 2014: Beyond Hopkinson’s bar. *Philosophical Transactions of the Royal Society A: Mathematical, Physical and Engineering Sciences*, **372**, no. 2023, 20130195–20130195, doi:10.1098/rsta.2013.0195.
- [32] Platzer, A., A. Leygue, L. Stainier, and M. Ortiz, 2021: Finite element solver for data-driven finite strain elasticity. *Computer Methods in Applied Mechanics and Engineering*, **379**, 113756, doi:10.1016/j.cma.2021.113756.  
URL <https://linkinghub.elsevier.com/retrieve/pii/S004578252100092X>
- [33] Priadi, D., C. Levaillant, L. Penazzi, E. Di Pasquale, and S. Aita, 1991: Introduction of strain rate effects in constitutive equations suitable for sheet metal stamping applications. *MECAMAT 91*, 1991.
- [34] Réthoré, J., 2018: *UFreckles*, doi:10.5281/zenodo.1433776.
- [35] Rossi, M., M. Badaloni, P. Lava, D. Debruyne, and F. Pierron, 2016: A procedure for specimen optimization applied to material testing in plasticity with the virtual

- fields method. *AIP Conference Proceedings*, AIP Publishing LLC, 200016.  
URL <http://aip.scitation.org/doi/abs/10.1063/1.4963634>
- [36] Rossi, M., P. Lava, F. Pierron, D. Debruyne, and M. Sasso, 2015: Effect of DIC spatial resolution, noise and interpolation error on identification results with the VFM: Effect of DIC spatial resolution, noise and interpolation on VFM identification. *Strain*, **51**, no. 3, 206–222, doi:10.1111/str.12134.  
URL <https://onlinelibrary.wiley.com/doi/10.1111/str.12134>
- [37] Seghir, R. and F. Pierron, 2018: A Novel Image-based Ultrasonic Test to Map Material Mechanical Properties at High Strain-rates. *Experimental Mechanics*, **58**, no. 2, 183–206, doi:10.1007/s11340-017-0329-4.
- [38] Stainier, L., A. Leygue, and M. Ortiz, 2019: Model-free data-driven methods in mechanics: material data identification and solvers. *Computational Mechanics*, **64**, no. 2, 381–393, doi:10.1007/s00466-019-01731-1.  
URL <http://link.springer.com/10.1007/s00466-019-01731-1>
- [39] Swift, H., 1952: Plastic instability under plane stress. *Journal of the Mechanics and Physics of Solids*, **1**, no. 1, 1–18.
- [40] Vinel, A., 2022: *Characterization of the thermomechanical behaviour of metals for high strain-rates, using ultra-high speed imaging cameras*. Theses, École centrale de Nantes.  
URL <https://theses.hal.science/tel-03954263>
- [41] Vinel, A., R. Seghir, J. Berthe, G. Portemont, and J. Réthoré, 2021: Metrological assessment of multi-sensor camera technology for spatially-resolved ultra-high-speed imaging of transient high strain-rate deformation processes. *Strain*, **57**, no. 4, e12381, doi:<https://doi.org/10.1111/str.12381>.  
URL <https://onlinelibrary.wiley.com/doi/abs/10.1111/str.12381>
- [42] Witz, J-F., P. Lecomte-Grosbras, A. Morch, C. Martel, F. Lesaffre, and M. Brieu, 2017: Digital image correlation for large strain. *International Digital Imaging Correlation Society*, Springer, 163–167.